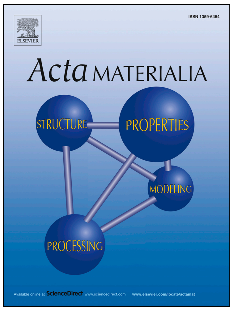

Hydrogen-enhanced fatigue crack growth in a single-edge notched tensile specimen under in-situ hydrogen charging inside an environmental scanning electron microscope

Di Wan, Yun Deng, Jan Inge Hammer Meling, Antonio Alvaro, Afrooz Barnoush

PII: S1359-6454(19)30175-2
DOI: https://doi.org/10.1016/j.actamat.2019.03.032
Reference: AM 15202

To appear in: *Acta Materialia*

Received Date: 11 November 2018
Revised Date: 9 March 2019
Accepted Date: 24 March 2019

Please cite this article as: D. Wan, Y. Deng, J.I.H. Meling, A. Alvaro, A. Barnoush, Hydrogen-enhanced fatigue crack growth in a single-edge notched tensile specimen under in-situ hydrogen charging inside an environmental scanning electron microscope, *Acta Materialia*, https://doi.org/10.1016/j.actamat.2019.03.032.

This is a PDF file of an unedited manuscript that has been accepted for publication. As a service to our customers we are providing this early version of the manuscript. The manuscript will undergo copyediting, typesetting, and review of the resulting proof before it is published in its final form. Please note that during the production process errors may be discovered which could affect the content, and all legal disclaimers that apply to the journal pertain.

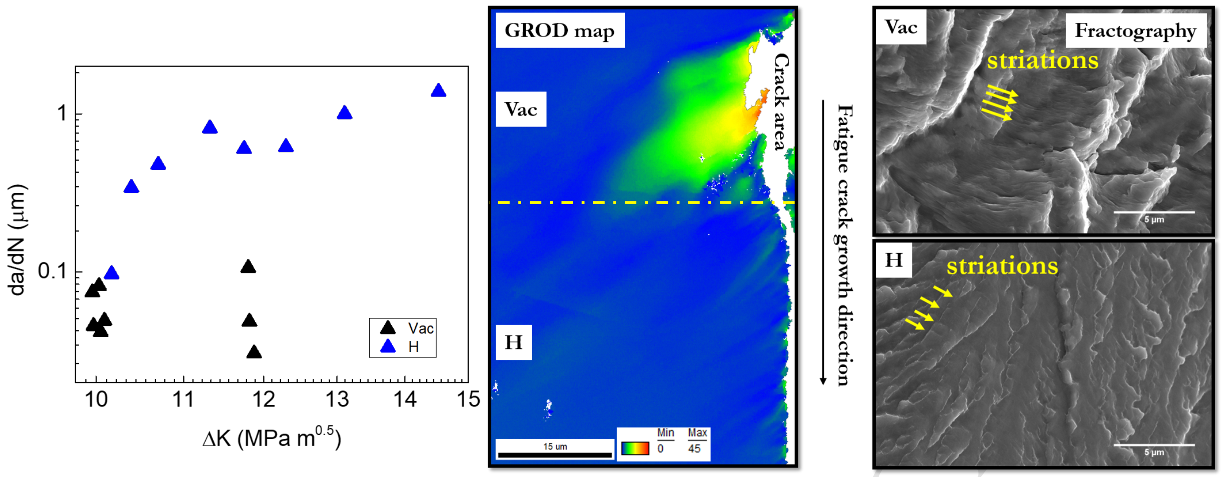
da/dN (µm)
1
0.1
10
11
12
13
14
15
ΔK (MPa m^0.5)
Vac
H
GROD map
Vac
H
Crack area
15 um
Min
Max
0
45
Fatigue crack growth direction
Vac
Fractography
striations
5 µm
H
striations
5 µm

Hydrogen-enhanced fatigue crack growth in a single-edge notched tensile specimen under in-situ hydrogen charging inside an environmental scanning electron microscope

Di Wan[1,*], Yun Deng[1], Jan Inge Hammer Meling[1], Antonio Alvaro[2], Afrooz Barnoush[1]

1. Department of Mechanical and Industrial Engineering, Norwegian University of Science and Technology, Richard Birkelands vei 2B, 7491 Trondheim, Norway.

2. SINTEF Industry, 7456 Trondheim, Norway.

Email: di.wan@ntnu.no

* Corresponding author

Abstract

Fatigue crack growth (FCG) test was done on a pre-cracked single-edge notched tensile (SENT) specimen with oligocrystalline ferritic structure. Innovative in-situ hydrogen (H)-charging by plasma inside an environmental scanning electron microscope (ESEM) was adopted to directly observe the H influence on the FCG behavior of this material. Diverse in-situ and post-mortem characterization methods including secondary electron imaging, backscatter electron imaging, electron backscatter diffraction (EBSD) and scanning probe microscopy (SPM) were used to investigate the material's behavior. It was observed that the crack growth rate was enhanced by about one magnitude when H was charged, in comparison with the reference test in vacuum (Vac). The FCG procedure was concluded as strongly associated with the plasticity evolution in the vicinity of the crack-tip. A simple model based on the restricted plasticity was proposed for the H-enhanced FCG behavior. A peculiar frequency dependency of the H-enhanced FCG behavior was observed at low loading frequencies (0.015 Hz ~ 0.15 Hz): under the same in-situ H-charging condition, a lower frequency gave a slower crack growth rate and vice versa. This behavior was explained by the thermally activated dislocation motion correlated with the plasticity shielding effect during crack growth.

Keywords: fatigue crack growth (FCG); hydrogen embrittlement; SENT specimen; EBSD; SEM.

1. Introduction

Hydrogen embrittlement (HE) has been discussed intensively for more than a century since the first document about the hydrogen (H) damage in iron and steels by Johnson in 1875 [1]. Several different mechanisms regarding various scales and aspects have been proposed, such as hydrogen-enhanced localized plasticity (HELP) [2-7], hydrogen-enhanced decohesion (HEDE) [8-11], adsorption-induced decohesion (AIDE) [12-15], hydrogen-enhanced vacancy production [16, 17] and hydrogen-induced phase transformation [18-21]. Among these mechanisms, the HELP and HEDE mechanisms gained the most attention based on diverse experimental proofs.

Another failure mechanism for engineering structures comes from cyclic loading which could lead to fatigue failure. This type of engineering failure was strongly linked to economic loss. According to statistics in 1983, the fatigue failures costed $119 billion per year from the US industry, and this number seemed to be meaningfully increasing in the recent years [22]. It is even worse when environmental conditions applied. For some large industrial structures, such as oil platforms in the sea, a combined effect of vibrational loading and extreme environmental conditions should be taken seriously. In some cases, small cracks could be formed in the structures, which lead to premature failure. As for engineers' prospect, it is of great importance to know how long the structure could still serve in such conditions without further repairing, and in academic point of view, the fatigue crack growth (FCG) behavior should be studied.

The combined effect from HE and cyclic loading has been intensively studied by a group of scientists from Kyushu University [23-28] using high pressure H_2 gas on various metals. Most of the embrittled specimens showed localized deformation at the crack-tips, and based on these investigations, a model called "hydrogen-induced successive crack growth (HISCG)" has been proposed [29]. This model adopted the slip deformation localization at the crack-tip, which was in accordance with the HELP mechanism, yielding suppressed crack-tip blunting and a faster crack propagation rate. Even though this model could explain some cases, important evidences are still missing [24]. One reason is that most of the investigation results were on materials with complex structures such as mixed phases, different grain sizes, various precipitates, etc. All the impurities in the materials could make the H-effect more difficult to be interpreted. A clear setup on clean and simple model material with least possible complexity should be proposed to support this model.

In the present study, a single-edge notched tensile (SENT) specimen was produced from an oligocrystalline ferritic Fe-3wt%Si steel and tested under low frequency cyclic loading in an environmental scanning electron microscope (ESEM) in both vacuum (Vac) condition and H-plasma charging condition. Oligocrystals are coarse-grained materials with only one grain existing through the thickness direction. By using oligocrystal, the behavior of material could be localized in a single grain and some complicated influence from crystal orientation or grain boundaries could be eliminated in certain extent. The FCG behavior was observed by the ESEM and analyzed with other scanning electron microscopy (SEM) techniques. The testing results gave a convincing proof of the HE effect from H-plasma charging and the possible mechanisms of H-enhanced FCG were discussed.

2. Materials and Experimental

The material used in this study was a Fe-3wt%Si ferritic steel. The chemical composition by weight percent is shown in Tab. 1. The raw materials were annealed at 1250 °C for four weeks followed by furnace cooling to facilitate the grain growth. The resulting material has pure ferritic structure and the final grain size is about 1~2 mm.

Tab. 1 Chemical composition of the investigated material.

Elem.	**C**	**Si**	**Mn**	**P**	**S**	**Cr**	**Ni**	**Mo**
wt.%	0.018	3.000	0.055	0.008	0.003	0.010	0.006	0.003
Elem.	**Cu**	**Al**	**Ti**	**Nb**	**V**	**B**	**Zr**	**Fe**
wt.%	0.013	0.015	0.001	0.002	0.001	0.0002	0.0010	Bal.

SENT specimens were cut from the heat-treated materials by electron discharge machining (EDM). The shape of the specimens is shown in Fig. 1. The specimen has the dimension of thickness *B* = 1 mm, width *W* = 6 mm and the gauge length *L* = 20 mm. A pre-crack (PC) with 1 mm length was introduced by cyclic three-point bending. Since the grain size is relatively large, only one grain exists through the thickness direction (oligocrystal). It should be noted that the tests and characterizations shown in the present paper were from a single exemplary specimen for the sake of keeping the constraints identical along the crack.

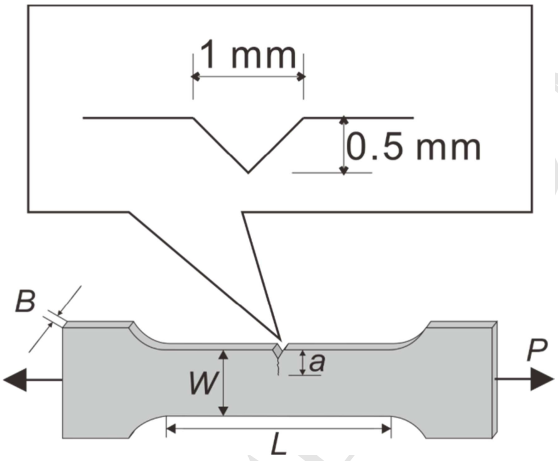

Fig. 1 The SENT specimen geometry and notch dimension.

Before testing, the specimen was characterized by electron backscatter diffraction (EBSD, Nordif EBSD system) in a Quanta 650 ESEM (Thermo Fisher Scientific Inc., USA) with an acceleration voltage of 20 kV at a working distance of about 10 mm. The normal direction inverse pole figure (ND-IPF) maps, kernel average misorientation (KAM) maps, and grain reference orientation deviation (GROD) maps were plotted over the region of interest (ROI). The results are shown in Fig. 2.

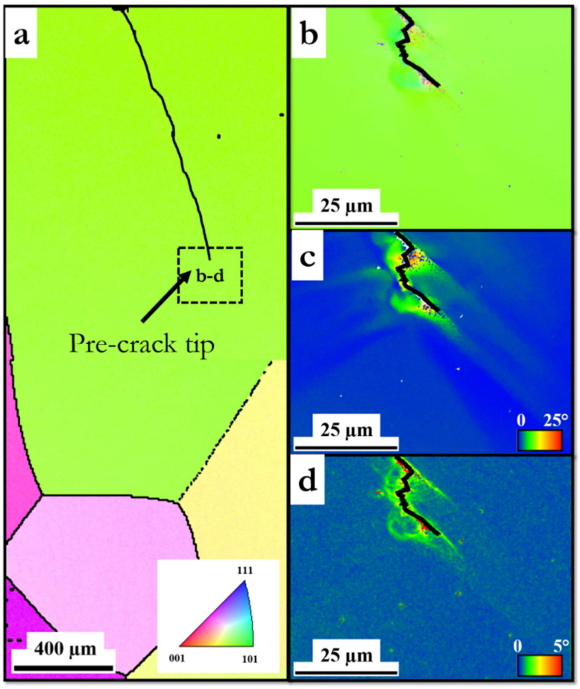

Fig. 2 EBSD maps of the investigated SENT specimen: a. ND-IPF map over the area near the PC; b. ND-IPF map over the PC tip; c. KAM map over the PC tip; d. GROD map over the PC tip. IPF maps have the legend shown in the orientation triangle. The color scale for a and b is the same.

The FCG test was done by a tensile/ compression module (Kammrath & Weiss GmbH, Germany) inside the ESEM. The specimen was loaded at load ratio $R = 0.5$. The tensile/ compression module was operated in a load-controlled mode with an intrinsic displacement-control nature of the device. The load range was chosen such that the stress intensity factor range (ΔK) was above the empirical threshold value (ΔK_{th}) obtained from preliminary tests and increased following the stage II according to Paris' law. The cyclic loading frequencies were 0.15 Hz and 0.015 Hz, which were denoted as low frequency (LF) and ultra-low frequency (ULF), respectively, in the following text. After every 100 cycles, the specimen was unloaded to 0 N for imaging to avoid possible elastic strain influence on the image. The ESEM was operated at 30 kV accelerating voltage. Both secondary electron (SE) images and backscatter electron (BSE) images were taken. The SE images were used to check the crack length and the topography near the crack, and the BSE images were controlled to an optimum channeling contrast to reveal the plastic deformation near the crack-tip. The crack growth rate was calculated from the measured crack length over the cycles interval (100 cycles).

For simplification, the ΔK during cyclic loading was calculated based on the SENT specimen described in Ref.[30]. It was assumed the crack in this test was a type I crack (opening mode), and the stress intensity could be calculated by Eq. 1:

$$K_I = \frac{P}{B\sqrt{W}} f\left(\frac{a}{W}\right) \qquad \text{Eq. 1}$$

in which *f* is a dimensionless function and reads as Eq. 2.

$$f\left(\frac{a}{W}\right) = \frac{\sqrt{2\tan\frac{\pi a}{2W}}}{\cos\frac{\pi a}{2W}}\left[0.752 + 2.02\left(\frac{a}{W}\right) + 0.37\left(1 - \sin\frac{\pi a}{2W}\right)^3\right] \qquad \text{Eq. 2}$$

where *W* is the width of the specimen, *B* is the specimen thickness, *a* is the crack length and *P* is the applied tensile load, as already indicated in Fig. 1.

The *ΔK* value is thus calculated by the following Eq. 3:

$$\Delta K = K_{\max} - K_{\min} \qquad \text{Eq. 3}$$

where $K_{\max}$ and $K_{\min}$ are the maximum and minimum K_I values, respectively, during one loading cycle.

H-plasma charging technique was applied to study the HE effect during FCG of the studied material. An Evactron plasma source (XEI Scientific, Inc., USA) was used to ignite and inject the plasma phase into the Vac chamber from a hydrogen gas source. The source hydrogen gas was produced by a hydrogen generator using electrolysis principle from pure water. The gas flow rate was 250 ml/min. The H-charging method was the same as described in Ref. [31]. According to the report from XEI Scientific Inc. [32], the H radicals created by the plasma source contained both H atoms and excited hydrogen gas molecules. During charging, the plasma phase was not injected directly on to the specimen surface, but only the active particles could still take part in the reaction. By this means, the specimen surface would have least possible damage from exposure to plasma. The charging conditions were kept constant during the whole test, and the loading condition could be measured and controlled precisely by the miniature testing module, indicating a well-constrained setup for the H-uptake. According to a previous work from the authors' research group [31], the fugacity of the dissociated H atoms can reach a value larger than 80 Pa in the vacuum chamber, and can even reach several MPa locally [33]. However, due to limited thermodynamics data in the plasma phase and the missing physics in the H uptake mechanism from plasma phase, only indirect values of the H concentration could be assumed.

Since the studied specimen has an oligocrystalline structure, the crack could grow a relative long distance with well-defined loading conditions. Furthermore, the relative stress conditions with respect to the neighboring grains could be kept almost unaffected during crack growth. Hence, we changed the environment during the test with keeping all other parameters unbothered to reveal the "pure" environmental influence. This means, both the reference test and the control test were done in the same grain under the same mechanical loading with only alteration in the environment.

The “in-situ” tests were done with in-situ loading and in-situ H-charging. In-situ imaging was partially possible when the H-plasma was switched off and the chamber was pumped to high Vac again. This was due to the technical limitations of the SEM detector. Normally about 10 s was required for the chamber to reach the high Vac state. Hence, the “in-situ imaging” here was limited to “in-situ in position” but “ex-situ in environment”.

After loading, the specimen was taken out and characterized by SEM including secondary electron imaging and EBSD to check the plastic deformation zone near the crack. Scanning probe microscopy (SPM) in a TI 950 Nanoindentation system (Hysitron Inc., USA) using a Berkovich tip was adopted to check the topography of the region near the propagated fatigue crack. The ROIs were in 8 µm x 8 µm squares and were from the representative characteristic regions near the main fatigue crack. The SPM images were processed by the open source software Gwyddion.

3. Results

3.1 Fatigue crack growth behavior

The crack length data were measured from the SEM images taken between loading cycles, and the *ΔK* values were calculated based on the SENT specimen assumption as described in the experimental section. The fatigue crack growth rate (FCGR, denoted as *da/dN*) vs. *ΔK* results were plotted on a logarithmic scale and shown in Fig. 3 as different comparisons. It is worth noting that the starting *ΔK* value was controlled to a value that was a little bit higher than the empirical ΔK_{th} from preliminary tests for this material and the FCG behavior in the Paris’ regime was expected from the present test. Fig. 3a shows the comparison between the Vac and H cases under ULF loading condition. The FCGR was slightly enhanced by H, but the enhancement was not very significant. While Fig. 3b shows the comparison under LF loading condition, and the FCGR was increased by about one magnitude when H was charged into the chamber. The comparison in Fig. 3c shows the frequency dependency of the H-enhanced FCGR. The LF loading condition gives a more significant FCGR enhancement by H.

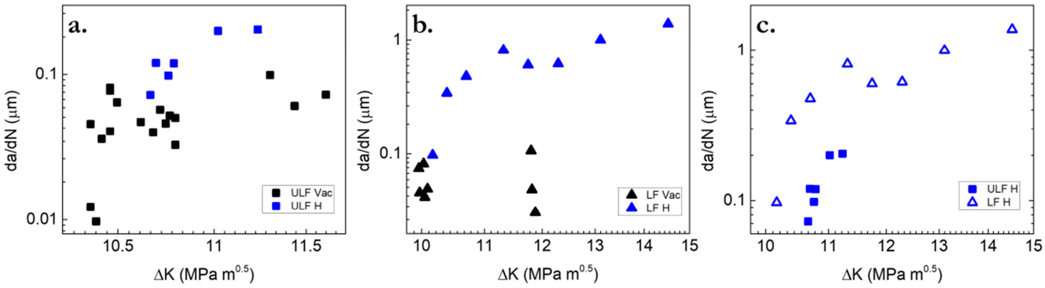

Fig. 3 Fatigue crack growth data of the investigated specimen: a. Vac and H cases under ULF; b. Vac and H cases under LF; c. H cases under ULF and LF.

3.2 Crack-tip characterization

The crack-tip during cyclic loading was characterized by SEM, including secondary electron (SE) imaging and backscatter electron (BSE) imaging. The results are shown in Fig. 4. The crack length increment (Δa) after the loading intervals of each 100 cycles was measured by comparing the present image with the image from the last loading step (not shown in the figures), which is shown by the yellow double-arrow lines in the SE images of Fig. 4. The ΔK range was calculated for each status based on the SENT specimen approach. The images showed the microstructure in the vicinity of the crack-tip resulted from the same ΔK range but under different environmental conditions. For both ULF and LF, the H-charged case had an accelerated FCGR of about 10 µm per 100 cycles, while the Vac case had the FCGR of only 3.3 µm and 4.9 µm per 100 cycles, respectively. The SE images mainly showed the topography near the crack-tip, which revealed the differences mainly in the deformation pile-ups. The crack grown in Vac was normally associated with more severe pile-ups near the crack-tip, and the lines from deformation were normally curves; while the crack grown in H had less pile-ups and the lines were straighter, when present. Moreover, the BSE images showed a stark contrast as contour lines in the vicinity of the crack-tip in Vac case (see the highlighted area in Fig. 4), but in contrast, the H case did not show such contrast. The BSE contrast is normally associated with atomic number contrast and crystal orientation contrast. In this large single-phase ferritic grain, atomic number contrast was almost uniform over the whole grain, and only orientation contrast should be considered from the BSE images. In the present study, these images could be used to evaluate the plasticity near the crack-tips.

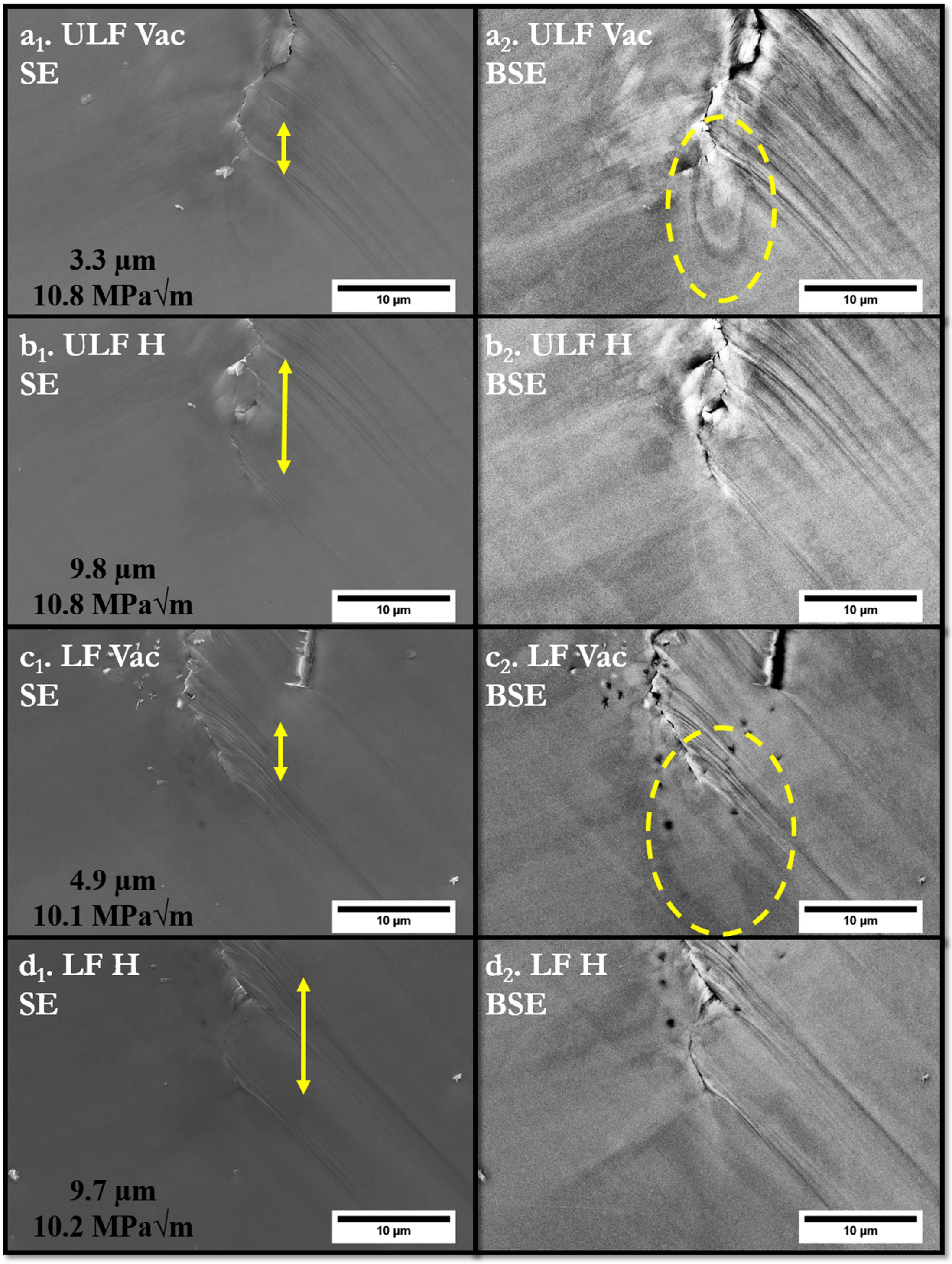
a1. ULF Vac
SE
3.3 µm
10.8 MPa√m
10 µm
a2. ULF Vac
BSE
10 µm
b1. ULF H
SE
9.8 µm
10.8 MPa√m
10 µm
b2. ULF H
BSE
10 µm
c1. LF Vac
SE
4.9 µm
10.1 MPa√m
10 µm
c2. LF Vac
BSE
10 µm
d1. LF H
SE
9.7 µm
10.2 MPa√m
10 µm
d2. LF H
BSE
10 µm

Fig. 4 Crack-tip characterization in different conditions as marked in each subfigure. The double-arrow lines indicate the crack advance during the loading segment of 100 cycles. The corresponding crack growth and ΔK level are marked in each subfigure. The left column (a_1 to d_1) shows the SE images and the right column (a_2 to d_2) shows the BSE images. The global FCG direction is from top to bottom for all subfigures.

3.3 EBSD post-characterization

The area near the fatigue crack was characterized by EBSD technique on the post-mortem specimen after loading. The resulting GROD maps were plotted for both ULF and LF loading conditions, respectively, and were shown in Fig. 5a and b. Different environmental conditions were separated by yellow dash-lines. Magnified representative featured areas on the left part of the crack were plotted in Fig. 5a$_1$, a$_2$ and b$_1$, b$_2$ with the same coloring scale. Since the GROD values were calculated based on the orientation deviation with respect to a reference orientation, this map was commonly used to evaluate the plasticity assuming the orientation change came from plastic deformation [24, 34, 35]. It is worth noting that the large plastic field in the top left corner of Fig. 5a came from the pre-cracking procedure, which was strongly associated with the crack initiation procedure, and this was not an area of interest regarding the present study. From Fig. 5, it was clearly shown that the fatigue fracture was associated with plasticity near the crack. The magnified views in Fig. 5 (a$_1$, a$_2$, b$_1$, b$_2$) were acquired with higher resolution on the plastic zones and showed that the patterns were periodic along the crack growth path. The regular patterns were extending along two different <110> directions on both sides of the crack, and the directions were the same for all conditions. When loaded with ULF, the material had a plastic extension of about 18~20 µm in Vac and 8~10 µm in H, respectively, away from the crack. While when loaded with LF, the plastic extension ranged from 22~25 µm in Vac and 4~8 µm in H, respectively. Fig. 6 showed the misorientation distribution versus the distance away from the crack in different conditions. The distributions along the highlighted lines in Fig. 6a$_1$ (ULF) and b$_1$ (LF) were plotted in a$_2$ and b$_2$, respectively. For both frequencies, one line-profile in Vac and two line-profiles in H were presented. The misorientation of the area loaded in Vac (about 25~30°) was much larger than that in H (up to 5° in LF and up to 15° in ULF). The red triangle in Fig. 6a$_1$ showed the peak misorientation in the H condition after ULF loading, which read about 15° from Fig. 6a$_2$. In the ROI of the LF case, no such strong peaks were found in the misorientation profile, and the maximum value was less than 5° from the data. The size of the plastic zone (considering high misorientation values) could also be evaluated from the profiles, which corresponded to the results mentioned in the above sentences.

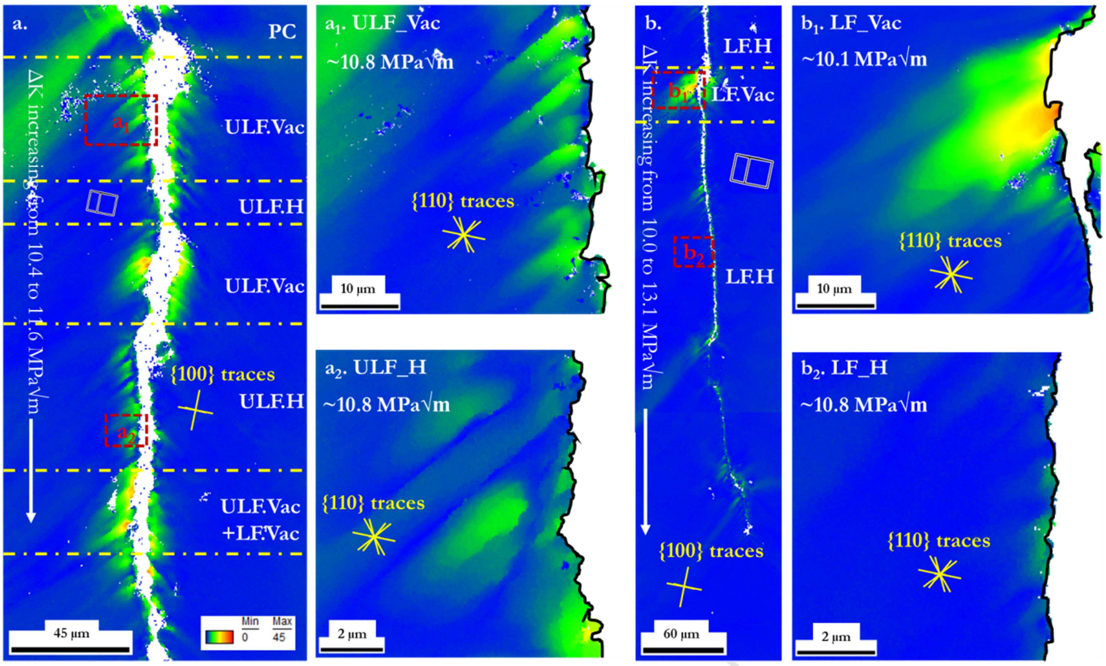

Fig. 5 GROD maps near the fatigue crack after loading with a. ULF (magnified ROIs: a_1. in Vac and a_2. in H) and b. LF conditions (magnified ROIs: b_1. in Vac and b_2. in H). The ΔK range for a is from 10.4 to 11.6 MPa√m, and that for b is from 10.0 to 13.1 MPa√m. The global FCG direction is from top to bottom. The color scale is the same for all sub-plots.

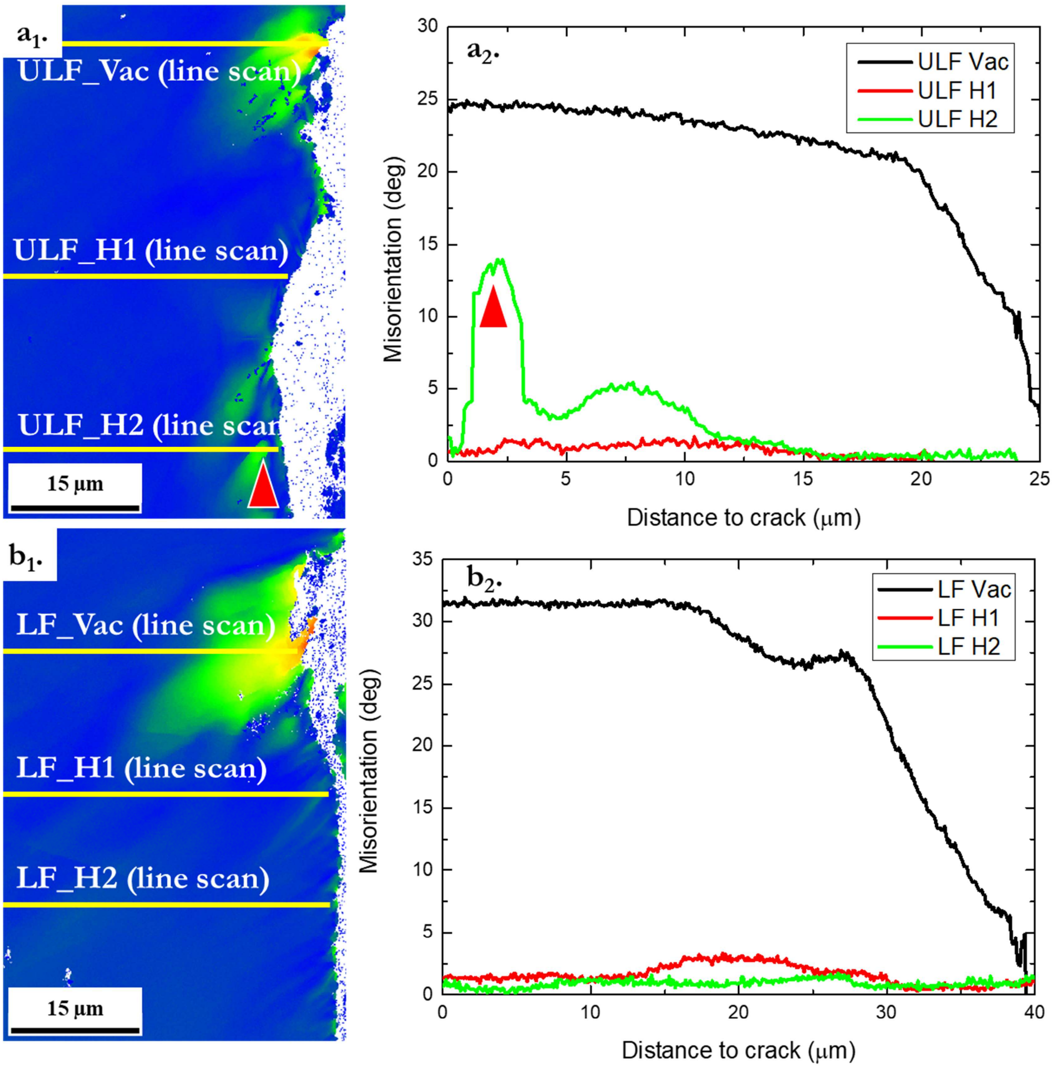

Fig. 6 GROD maps and misorientation distribution focusing on a. ULF loading and b. LF loading; a_2 and b_2 are the misorientation distribution profiles showing the highlighted lines in a_1 and b_1, respectively. The red triangles in a_1 and a_2 are indicating the same misorientation peak. The global FCG direction is from top to bottom. The color scale of the EBSD maps is the same as in Fig. 5.

3.4 Topography near the fatigue crack

The SPM technique was adopted to check the topography of the area near the fatigue crack. Fig. 7 showed the constructed 3D images of the representative areas under different loading conditions. The two areas were taken from the area next to both sides of the fatigue crack. It is clear that the material near the crack formed a topographical roughness with different heights ranging from 10~30 nm in the ROIs from different loading conditions. The roughness is the result from the dislocation slipping, as noted by

Vehoff and Neumann [36] in the similar Fe-Si system. The slip lines resulted from loading in Vac (Fig. 7a and b) were generally higher than that resulted from loading in H (Fig. 7c and d). The Vac conditions with both frequencies gave a final roughness in the range of 30 nm while the H conditions gave a less pronounced roughness of about 10~20 nm. The slip lines were denser in LF conditions than in ULF conditions. Considering the distance between the grooves of the roughness in the Vac cases, the ULF case had a larger value of about 3~4 µm while the LF case had only 1~2 µm between each slip line. In the H cases, the slip lines were not extending over the scanned area, and this parameter could not be compared directly. However, the slip lines localized near the crack (Fig. 7c and d) gave a value of about 1 µm for both ULF and LF cases.

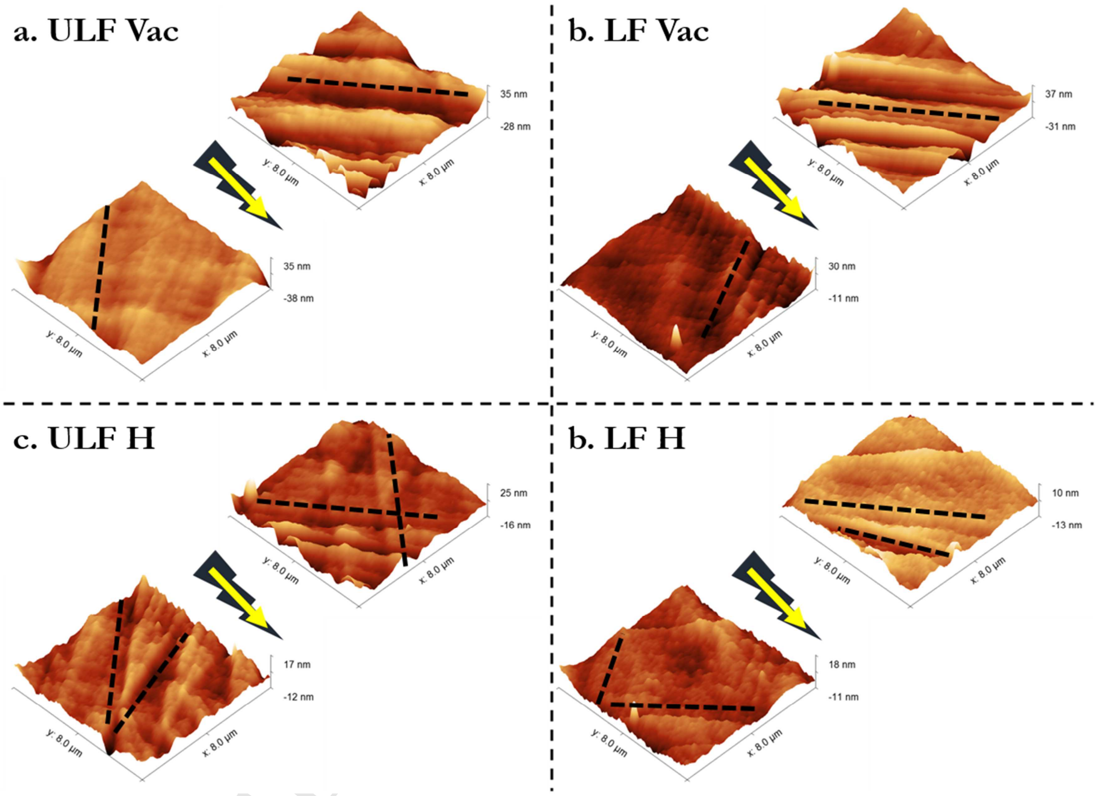

Fig. 7 SPM images on characteristic regions near the main fatigue crack a. ULF Vac, b. LF Vac, c. ULF H, d. LF H. The arrows represent the global FCG direction and the relative position of the crack. The dash lines in the sub-plots denote the directions of the slip lines.

3.5 Fractography

After the specimen has been completely fractured, the fracture surface was investigated by SEM. The fracture features were in general the same along the thickness direction of the SENT specimen, which means the test could be considered as done on a two-dimensional oligocrystal. Thus, some loading complexities could be constrained. In the present results, the crack length data could be correlated to the fracture surface features thanks to the accurate measurement at each loading step. Consequently, the loading parameters as well as the environmental conditions could also be correlated. It could be seen from Fig. 8a that the overall fracture features looked differently regarding different loading and environmental conditions. The whole grain was fractured transgranularly, however, essential differences in the fracture surface that was subjected to different testing conditions could be clearly discerned, as shown in Fig. 8. The striations formed in Vac were densely arranged perpendicular to the FCG direction with the protuberances smooth and round, as illustrated in Fig. 8b and c. While the striations formed in H environment were sparsely distributed and form some brittle-like facets, as shown in Fig. 8d and e. Furthermore, the directions of the striations in general were forming a roughly 45° to the global FCG direction, according to the measurement in the figures. The protuberances look sharper than the Vac case, and the overall surface looked flatter than that of the Vac case. The spacing between the major striations were measured from the magnified fractographs in Fig. 8. Under ULF loading, an average spacing of 0.09 µm and 0.74 µm were obtained for the Vac and H cases, respectively. While for LF loading, the value of 0.10 µm and 0.84 µm were obtained for the Vac and H cases, respectively. These values fit well with the data in Fig. 3 except the ULF H case. However, one could also see some denser striations in the ULF H case besides the characteristic "quasi-cleavage" striations, as highlighted by a black rectangle in Fig. 8d with a magnified subsection from it, which was not counted in the measurement. It is thus reasonable to consider the striation spacing corresponds well to the globally measured FCGR. By comparing the fracture features in different loading frequencies, no significant differences could be observed.

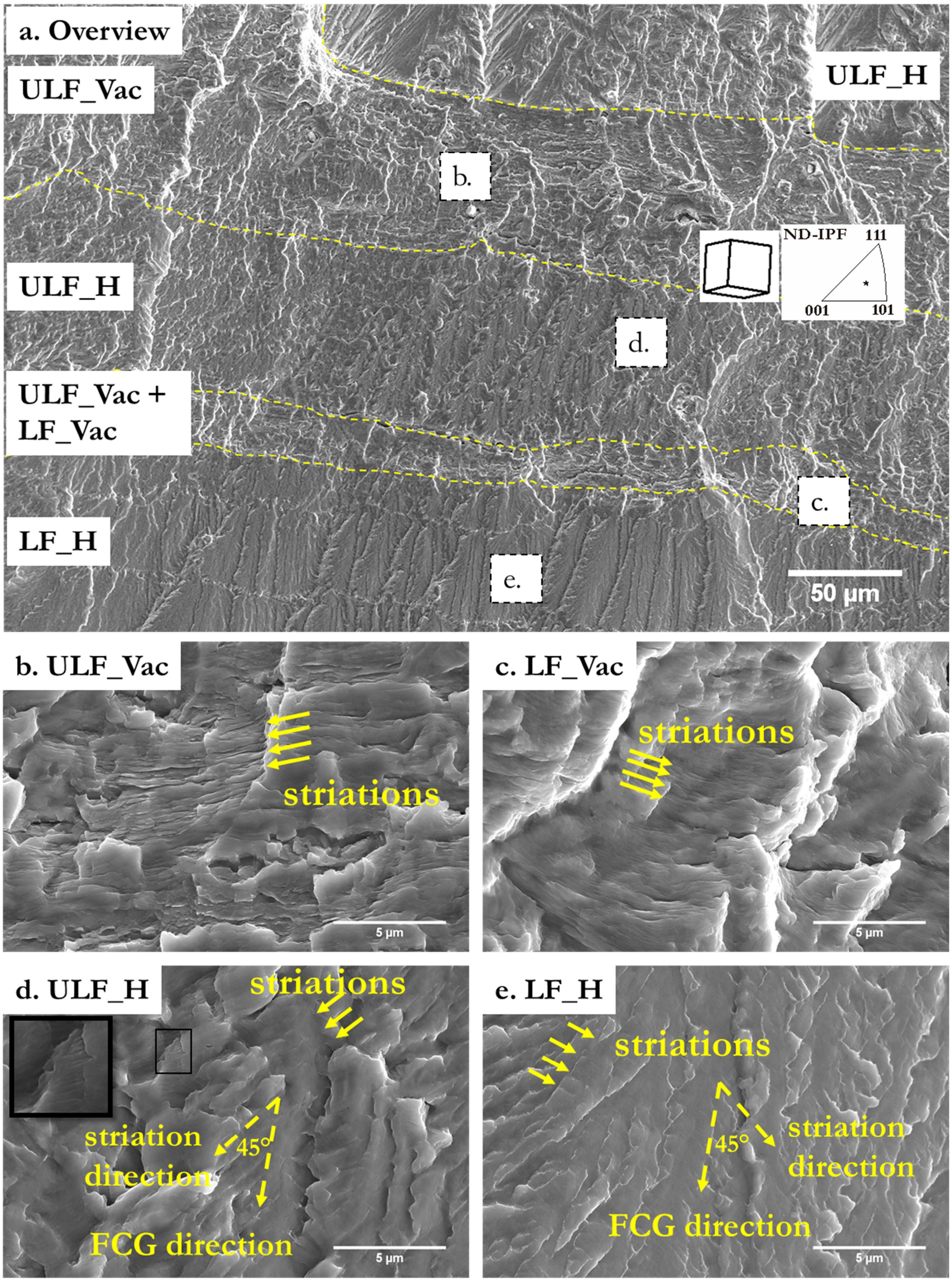
a. Overview
ULF_Vac
ULF_H
b.
ND-IPF
111
001
101
ULF_H
d.
ULF_Vac +
LF_Vac
c.
LF_H
e.
50 µm
b. ULF_Vac
striations
5 µm
c. LF_Vac
striations
5 µm
d. ULF_H
striations
striation
direction
45°
FCG direction
5 µm
e. LF_H
striations
45°
striation
direction
FCG direction
5 µm

Fig. 8 Fracture surface with features from different loading and environmental conditions (a. overview; b. ULF, Vac; c. LF, Vac; d. ULF, H; e. LF, H). The global FCG direction is from top to bottom. All the ROIs are in the same grain and the representative unit cell with the ND-IPF on this grain is shown in a.

4. Discussion

4.1 Plasticity-related fracture procedure

Based on the microstructure observation near the fatigue crack, it could be inferred that the FCG procedure was a plasticity-related procedure both in Vac and with H-charging. Before FCG, the notched specimen was subjected to cyclic loading to initiate the fatigue pre-crack. A certain plastic deformation zone was produced during this procedure. This plasticity could be observed in the upper left corner of Fig. 5. Due to text length concerns, the crack initiation procedure would not be discussed in this work and only the stable crack growth stage was considered.

Depending on the material's properties and loading conditions, the externally applied energy could be released either by crack growth (new surface opening) or by plastic deformation (e.g. dislocation motion, mechanical twinning or phase transformation), or in most cases by mixed mode of both of them. The experimental observations of a relatively larger plastic zone and a smaller crack advance in Vac case indicated that the energy was largely released by plastic deformation mechanisms. Since no phase transformation or mechanical twinning was observed in the studied material, it was inferred that the outwards dislocation motion into the material matrix from the crack-tip gave a significant contribution to the plastic energy release. As a result, fracture surface in Vac case showed a large plastic zone (Fig. 5 and Fig. 6) and a small crack advance (smaller striation distances as in Fig. 8b and c). According to Laird and Smith [37], the fatigue striations formed on the fracture surface are a result of blunting and sharpening of the crack tip under cyclic loading via a plastic deformation mechanism. This can confirm that the FCG in the current study is a plasticity-related procedure.

Based on the discrete-dislocation plasticity simulation results by Chakravarthy and Curtin [38], noticeable dislocations slipping could be observed around the crack-tip during crack growth, and the local strain field could extend to several microns away. Conventional large-scale investigations such as optical microscopy could capture the fracture or mechanical behavior at macro-scale but were difficult to reveal the quantitative measurement of the small-scale local strain. The micro-scale characterizations in this work, however, could successfully capture the plasticity at this level. Combining with EBSD technique, some quantitative crystallographic and microstructural data could also be obtained. In this test, the plasticity extension could range to about 30 μm in Vac, with a crystal rotation (misorientation) up to 30° based on the measurements shown in Fig. 5 and Fig. 6, depending on the loading conditions. This investigation gave strong proof to the simulation results in [38] that the FCG procedure was associated with plasticity evolution in the vicinity of the crack-tip.

When dislocations are introduced into the crack system, there is an effect named dislocation shielding, simply describing the phenomenon that dislocations are trying to lower the stress of the crack-tip. As is generally accepted, the vicinity of a crack-tip is often highly stressed. The shielding dislocations are thus emitted from the crack-tip and move into the material matrix and in this way make the crack blunt and thus lower the stress state at the crack-tip. However, dislocations also interact with themselves if they are emitted. A large amount of dislocations ahead can also restrict the new dislocations from emitting, therefore, the dislocations will accumulate in the nearby area close to the crack path but not extend into the matrix infinitely. When the shielding dislocations are sufficient to prevent new dislocations from emitting, the stress state will again be elevated by the external loading and thus the crack grows after the critical stress condition is reached. This mechanism could explain why we see discontinuous plastic zones along the crack path.

4.2 The HE effect from H-plasma charging

In a previous study [31], the HE effect on the same ferritic alloy was observed by H-plasma charging during slow strain rate tensile tests. With monotonic loading, the global elongation (final elongation value in percentage up to complete fracture) was reduced by about 5% in comparison with the reference test in Vac. The reasons were given as the combined effect from localized deformation and localized H-concentration. Following this conclusion, a notch was introduced and a sharp fatigue crack was initiated from the notch by cyclic loading, which could give a stress-concentrated location and thus controlling the crack path. From the FCG results, the H-charging by the plasma phase did take part in the FCG behavior, giving an increase of about one in magnitude of the FCGR. This result could be used as a confirmation to our previous proposal and a convincing proof of the HE effect from H-plasma charging.

As a direct comparison, the resulting fatigue fractography from H-charging in Fig. 8 was comparable with that under monotonic tensile loading in Ref. [31], with the only difference from fatigue striations. The characteristic “quasi-cleavage” facets were observed in the H-charged case in both works, c.f. Fig. 8 and Fig. 9. Previous literature showed similar H-induced “quasi-cleavage” features in various Fe-based BCC alloys under different H-rich environments [24, 39-46]. It is thus considered that one characteristics by H-charging in fractography is the “quasi-cleavage” fracture features.

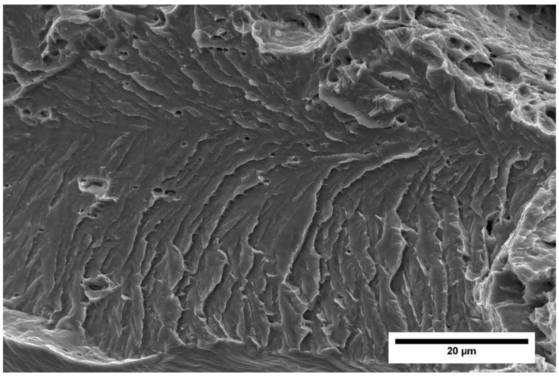

Fig. 9 Fracture feature with monotonic tensile loading with H-plasma charging on the investigated material, from Ref. [31].

The "quasi-cleavage" feature after H-enhanced FCG in a pure iron specimen was studied in a recent work [47]. They observed the "quasi-cleavage" regions were parallel to the {100} planes and concluded the H-enhanced FCG was due to the contribution of local cleavage fracture. However, this proposal contradicts our results. Based on our investigations, the fatigue crack did not change direction significantly during the whole test, either in Vac or in H. From the EBSD scans, the FCG direction was closer to {110} traces rather than {100}, as marked in Fig. 5a. From the crystallographic analysis, the ND of the fracture surface was approximately parallel to the crystallographic <1 3 5> direction, which did not correspond to the cleavage fracture surface of this material. Several reasons could attribute to this difference. The investigated material in [47] was a polycrystalline pure iron, the cleavage fracture could be activated due to local stress state and local crystal orientation accompanied by accommodations between grains. Furthermore, only selected grains were indexed in [47] with the cleavage orientation relationship, which did not contribute much to statistics. Another important factor was the stress state. The investigation area in [47] came from the mid-thickness of the CT specimen, which was experiencing more plane-strain condition. While most of other works including the present one focused on the surface area which was experiencing more plane-stress condition. This could give some differences since the plane-strain condition gave higher lattice dilatation. Under plane-strain condition, the material experienced a higher hydrostatic stress, and this stress state was a major reason for the elastic volume expansion, which could lead to a locally higher H-concentration. Therefore, a stronger HE phenomenon (cleavage fracture feature) was expected.

The previously proposed models for the H-enhanced FCG were mainly based on the HELP mechanism assumptions, which emphasize that H is aiding the deformation processes by enhancing the mobility of dislocations, and consequently making the plastic deformation zone smaller in size (e.g. [2, 7]). However, based on our investigations, there is no clear proof of enhanced dislocation mobility, but instead, a restricted mobility of dislocations seems to be more evident. It is observed that both the size of the deformation zone and the total amount of plasticity were smaller in the H cases comparing with the Vac cases, as was also pointed out in [47]. The misorientation distribution in Fig. 6a_2 and

b_2 showed this relation clearly. The maximum misorientation angle values were in general much smaller in the H cases than that of the corresponding Vac cases. If we consider the plasticity was only “localized”, a stronger plasticity, i.e. higher misorientation angle than the maximum value in the Vac case, should be observed when it gets closer to the crack. However, this was not the case based on the EBSD results. In another way, the misorientation profile, i.e. plastically deformed area, was strongly suppressed by H in comparison with the Vac cases. The same story could be told from the SPM results in Fig. 7 as well. The scanned areas were directly from the region connecting the primary fatigue crack, and no strong peaks could be seen in the H cases. This means the plasticity was impaired during the FCG in H. The reduced plastic zone by H was also confirmed by in-situ micro-cantilever bending test in the case of monotonic loading and step-wise loading in other BCC materials [48-50].

Based on the investigation from both fractography and plastic zone characterization, a model on the H-enhanced FCG was proposed. Fig. 10 is a schematic of the proposed mechanism. When a pre-crack is under cyclic loading, the loading would give contribution to both crack growth and plasticity independent of H influence. The cracking is considered as atomic plane separation (fast brittle cracking) while the plastic response results in deformation zones with higher misorientation (dislocation shielding and slow ductile cracking). It has been calculated by atomistic simulations that the strong trapping sites of H are distributed around the dislocation cores [51]. As an interstitial solid solute atom, H in general has a pinning effect on dislocation slipping, which will increase the critical resolved shear stress of some specific slip systems [52, 53]. Consequently, by impairing the mobility of the dislocation in hydrogen enriched volume in vicinity of the crack, the dislocation shielding effect on the stress intensity of the crack will be reduced in comparison with the H-free case such that the plasticity extension is smaller in H than in Vac (see the middle illustration in Fig. 10). The investigation results of the plastic zone size in the early section give convincing proof to this proposed mechanism. Another feature is the distribution of the plastic zone. The H-free case gives a more concentrated deformation zone while the H case gives more separated plastic zones (c.f. Fig. 5 and Fig. 6). This could be explained by the right-side illustration in Fig. 10 that the dislocation shielding effect is competing with the crack growth. Since the dislocation shielding is restricted by H, the extended distance of the plastic zone in the H case is shorter than that in the H-free case. A locally higher stress intensity at the crack tip is expected when the dislocation shielding on crack is restricted. Therefore, the critical stress state for crack growth is more easily reached in H than in Vac. In the assumptions, it is considered that the crack growth is free of plastic behavior, and thus, a larger undeformed distance between the plastic zones in H than in Vac could be seen. Hence, as a short conclusion, the mechanism of H-enhanced FCG is proposed as the H-restricted dislocation shielding and thus enhanced cracking.

Furthermore, as was also observed in Inconel 718 alloy [54], a secondary slip system would get more easily activated when H is present during the FCG procedure. According to our investigations, a secondary pile-up direction was observed in the H-charged case while no similar traces were found in the Vac case (c.f. Fig. 7). In the Vac case, the primary slip system was activated by the local stress intensity *K*, and the dislocations could partly shield the local *K* by the dislocation motion along the activated slip system. However, when H was present, the dislocation mobility was impeded based on our assumptions. Therefore, the local *K* was less shielded and this stress intensity could further activated new slip systems. The influence from a secondary slip system would also confine the motion of the primary slip system, which gives a more restricted dislocation shielding effect and thus less-extended plastic zone in the H case. This might be another mechanism of the restricted plasticity.

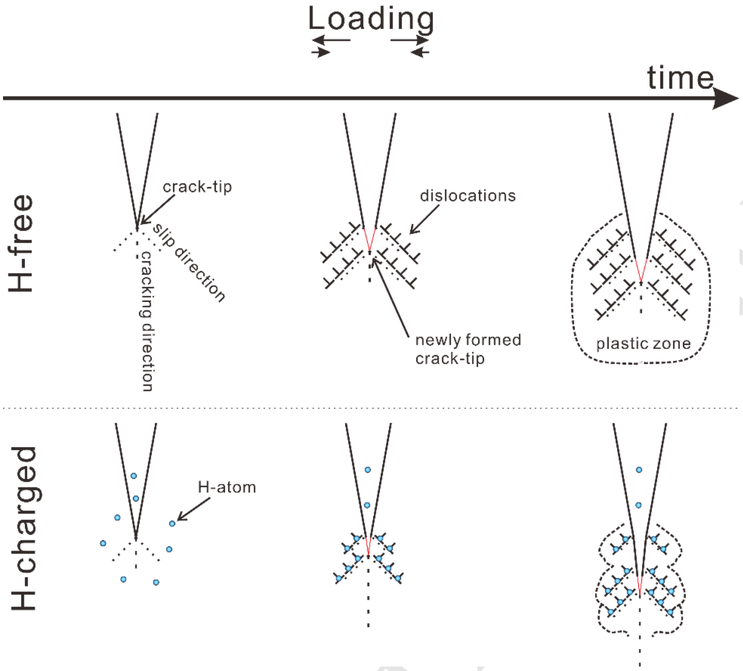

Fig. 10 Proposed H-enhanced cracking mechanism. Explanation in text.

4.3 Frequency effect

Typically, increasing the frequency of cyclic loading affects the kinetic of hydrogen uptake at the crack tip and reduces the FCGR of metals in a wide range. Consequently, a lower frequency leads to a higher FCGR. However, when it comes to a very low frequency range, this relation can deviate. Matsunaga et al.[28] did FCG tests on steels under high pressure H_2 gas with a wide range of loading frequency and found that when the frequency is higher than 0.1 Hz, the FCG acceleration in 0.7 MPa H_2 gas is decreasing with increasing frequency; while when the frequency is in the range of 10^{-3} Hz to 0.1 Hz, this relation is reversed. This result agrees with the result in the present study. In this work, two loading frequencies were adopted as ULF (~0.015 Hz) and LF (~0.15 Hz) that fall in the range of the peculiar frequency dependency range. As can be seen from Fig. 3, when tested in Vac, the frequency did not give strong influence of the FCGR, but during H-charging, the FCGR was clearly accelerated and this increment was depending on the frequency. The LF gave an acceleration about one magnitude in the FCGR, but the ULF gave a less acceleration.

The mechanisms of this peculiar frequency effect on H-enhanced FCGR in steels have been discussed in several different works [28, 55, 56]. This dependency was concluded to be attributed to the distribution of H concentration, i.e. local H-gradient, in the vicinity of the crack-tip, which affects the HELP process in the crack-tip zone. The basic idea was built on the assumption that a local steep gradient of H-concentration will result in the slip localization at the crack-tip. At ULF, the H has relatively more time to diffuse deeper into the material's matrix, which gives a smoother H-concentration profile. Assuming that the same H-concentration in the environment and the same crack-tip is under a higher loading frequency, the H diffuses less into the material, which means that in the vicinity of the crack-tip, the H-concentration is decreasing strongly as the distance to the crack-tip increases and consequently giving a local steep gradient of H-concentration. From the basic assumption, the local steep H-concentration gradient will make the dislocation slip behaviors more localized at the crack-tip (basic HELP mechanism) and thus leading to less crack blunting and faster crack advancement. Based on the assumptions, this model could explain the peculiar frequency dependency to an extent, but the detailed embrittlement mechanism seems to be a black box and remains unclear. To understand the possible mechanisms, three scenarios can be presented regarding a) the H concentration gradient, b) the H uptake and c) the H influence on the dislocation motion.

a) H concentration gradient

Based on the analytical model presented by Sofronis and McMeeking [57], the H profile ahead of the crack-tip is not monotonic, but instead, the peak concentration would appear some distance away from the tip, which was calculated to be 1.53 times of the crack opening displacement. Kotake et al. [58] updated this model by including the case under cyclic loading at load ration $R = 0.5$, which is corresponding to the present study. In the updated model, the loading time effect was also considered: longer time (lower frequency) gives higher peak concentration at full loading, but at the end of the unloading (to 0.5 of the maximum load) the concentration is lower. That is to say, lower frequency gives a larger amplitude of the H concentration value. The scenario could be schematically presented as Fig. 11. The Y-axis is the relative concentration ratio C_L/C_0 (local H concentration C_L over the constant initial concentration C_0). The X-axis is the relative distance to the crack-tip X/b (X is the absolute distance and b is the crack opening displacement as shown in the corner of Fig. 11). However, the calculation results from [57] and [58] do not give a significant different between the concentration resulting from ULF and LF loading. Considering the loading time effect on the H concentration resulting from 100 s loading and 10 s loading (which are in the similar magnitude as the presented study), there is a difference of roughly 10% in the peak H concentration. This value, however, seems to be insufficient to cause one magnitude different FCGR and such significant plasticity difference in the fracture process zone. Furthermore, due to the sharpness of the studied crack-tip, the crack opening displacement should be in the range of less than 1 µm. According to the above-mentioned model, the peak H concentration happens about 1~2 µm away from the crack-tip. This value does not necessarily agree with the measured plastic zone size. As a short summary, the effect from stress-controlled local H concentration could not satisfactorily explain the whole story.

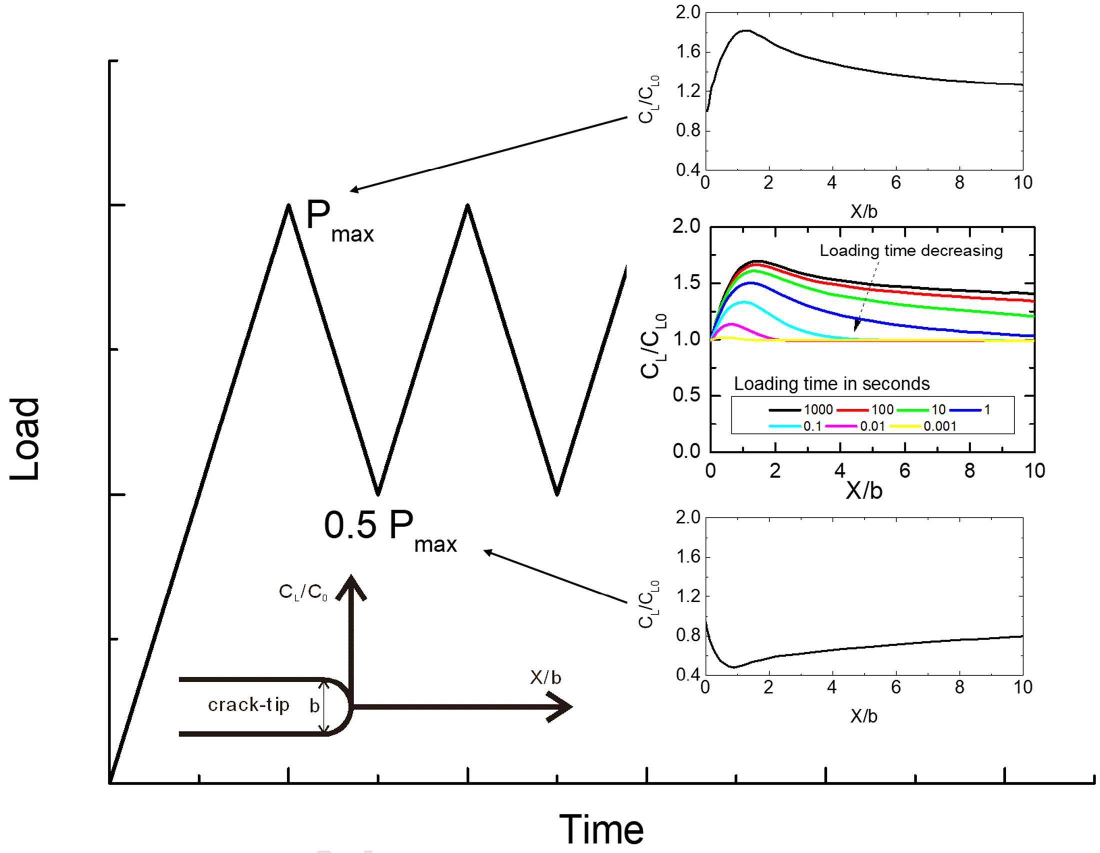

Fig. 11 Local H concentration profile at the crack-tip area during cyclic loading with the loading time effect on the profile. Concentration profiles adopted from [58].

b) H uptake

The major factor controlled by the frequency is the loading time difference. And the most possible consequence from this difference seems to be the H diffusion and uptake into the fracture process. If the surface H uptake is a controlling factor in this process, a higher H concentration is expected at ULF and thus a more significant embrittlement effect. However, this did not happen in our case nor in the study in [28]. Furthermore, by adopting the diffusion calculations, the time needed for H diffusion into the fracture process zone of several tens of microns is in the magnitude of 0.001 s, which can be fully covered by any single cycle in the current study. On the other hand, due to the relatively low solubility limit of H in BCC ferrite (atomic solubility of about $5*10^{-8}$, according to [59]), the fracture process zone was reasonably assumed to be saturated with H during the test. Hence, it is concluded that the H uptake situation should be similar for both the ULF and the LF cases, and is not the controlling factor in the embrittlement dependency on loading frequency.

c) H influenced dislocation motion.

When the above-mentioned points are somehow ruled out, we try to think about the fundamental theory of dislocation motion with the influence from strain rate since fundamentally we had a different displacement rate (more physically a different strain rate) during the test. From the classical theory, dislocation motion is associated with a thermally activated process that is dependent on the strain rate [60]. The higher the strain rate is, the lower thermal activation energy could be provided, and namely a higher external force is needed to move the dislocations. Consequently, higher strain rate hardens the material and lower strain rate softens the material. This relation could be expressed by the following empirical equation:

$$\dot{\varepsilon} = \dot{\varepsilon}_0 \exp\left(-\frac{\Delta G}{kT}\right) \qquad \text{Eq. 4}$$

where $\dot{\varepsilon}_0$ is a constant initial strain rate depending on the material system, k is the Boltzmann constant and T is the temperature. The macroscopic plastic strain rate $\dot{\varepsilon}$ could then be directly linked to the thermal activation energy ΔG for dislocation motion. From this relation, a higher strain rate leads to a smaller thermal activation energy and vice versa, when all other parameters keep constant. From a perceptual aspect, a lower strain rate means more time for dislocation jumping over the barrier and easier dislocation slipping and thus leading to a softened material, while a higher strain rate means more difficult dislocation motion and thus a harder material. Considering the testing conditions in the present study, the ULF condition (lower strain rate) gave a higher thermal activation energy, which gave the dislocations more chance to overcome the energy barrier for movement, compared to the LF condition. Quantitatively, there is a difference of about $kT \cdot \ln 10$ in the thermal activation energy. When no H is presented, this amount of difference seems insufficient to cause such a difference (the plastic zone sizes in ULF Vac and LF Vac cases are similar, c.f. Fig. 5.). Back to the proposed model in the above section, H has the effect of restricting dislocation motion, which makes the energy barrier larger. The ULF condition seems to lead to a higher thermal activation energy such that dislocations overcame the H enhanced barrier, while in the LF condition, a relatively lower thermal activation made dislocation motion less possible and thus a restricted plastic zone was observed. Based on the data with a wider frequency range in Ref. [28], a continuously weaker HE effect was observed when the frequency went lower from 0.1 Hz to 10^{-3} Hz. By ruling out the H diffusion as well as the H distribution in the system, the thermal activation process of dislocation motion in combination with the hydrogen impaired mobility of the dislocation seems to be the most successful mechanism to explain the peculiar frequency dependency of the H-enhanced FCGR at low frequency range. Analytically, this relation is shown in Fig. 12. At lower frequency range, the dislocation kinetics becomes a controlling factor that influences the HE effect, while when the frequency becomes higher, the H diffusion problem comes into play and the HE effect is mainly dependent on the diffusion. At the intersection range (about 0.1 Hz from [28]), the H-enhanced FCGR gets its peak enhancement. To prove this proposal, researchers in the numerical methodology fields are encouraged to shed some light on it.

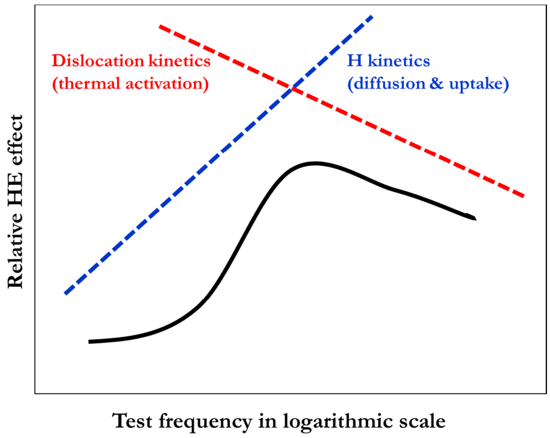

Fig. 12 Schematic description of the frequency dependency and the influencing factors. Solid line is the HE effect from the FCGR ratio in [28]. Red dash-line represents the thermal activation process influence and blue dash-line represents the H diffusion influence.

It should be noted that the form of H (diffusible H or trapped H) was not differentiated in the current study. From the presented scenarios, the effect of the enhancement in FCGR is more possibly coming from the trapped H because the diffusion and uptake mechanisms can be ruled out. However, due to the current technical limitations, the exact form of H in the vicinity of the crack-tip was not validated and only the possible assumptions are presented in the current study.

5. Conclusions

A SENT specimen with large grained ferritic structure was tested under low frequency cyclic loading in an ESEM with in-situ H-plasma charging and in Vac. The FCG behavior was observed by SEM. Some conclusions could be drawn as follows:

- The plasticity evolution in the vicinity of the crack-tip plays a dominating role in the FCG of the studied Fe-3wt%Si steel. The dislocation shielding effect on the crack could influence the FCGR.
- In H-plasma, the FCGR was enhanced by about one magnitude when compared with the FCGR in Vac with the same loading parameters.
- A mechanism on the H-enhanced FCG process was proposed based on the constrained dislocation shielding effect. The plastic zone near the crack-tip was restricted by the H-charging.
- In the tested frequency range (0.015 ~ 0.15 Hz), a higher frequency gave a higher FCGR value in H and vice versa. While in Vac, the frequency did not play a

significant role. The frequency dependency of the HE effect was explained by the competition between thermally activated dislocation motion and the H diffusion.

Acknowledgement

This study was financially supported by the Research Council of Norway through the HyF-Lex project (Petromaks2 Programme, project number 244068/E30).

Reference

[1] W.H. Johnson, On Some Remarkable Changes Produced in Iron and Steel by the Action of Hydrogen and Acids, Proc. R. Soc. London 23(156-163) (1875) 168-179.
[2] C.D. Beachem, A new model for hydrogen-assisted cracking (hydrogen "embrittlement"), Metall. Mater. Trans. B 3(2) (1972) 441-455.
[3] H.K. Birnbaum, P. Sofronis, Hydrogen-enhanced localized plasticity—a mechanism for hydrogen-related fracture, Mater. Sci. Eng., A 176(1-2) (1994) 191-202.
[4] I.M. Robertson, The effect of hydrogen on dislocation dynamics, Eng. Fract. Mech. 64(5) (1999) 649-673.
[5] I.M. Robertson, H.K. Birnbaum, An Hvem Study of Hydrogen Effects on the Deformation and Fracture of Nickel, Acta Metall. 34(3) (1986) 353-366.
[6] I.M. Robertson, H.K. Birnbaum, P. Sofronis, Hydrogen Effects on Plasticity, in: J.P. Hirth, L. Kubin (Eds.), Dislocations in Solids, Elsevier, Amsterdam, 2010, pp. 249-293.
[7] S. Wang, A. Nagao, P. Sofronis, I.M. Robertson, Hydrogen-modified dislocation structures in a cyclically deformed ferritic-pearlitic low carbon steel, Acta Mater. 144 (2018) 164-176.
[8] R.P. Gangloff, Critical issues in hydrogen assisted cracking of structural alloys, in: S.A. Shipilov, R.H. Jones, J.-M. Olive, R.B. Rebak (Eds.), Environment-Induced Cracking of Materials, Elsevier, Amsterdam, 2008, pp. 141-165.
[9] W.W. Gerberich, P.G. Marsh, J.W. Hoehn, Hydrogen Induced Cracking Mechanisms - Are There Critical Experiments?, in: A.W. Thompson, N.R. Moody (Eds.), Hydrogen Effects in Materials, Minerals, Metals & Materials Society (TMS), Warrendale, Pennsylvania, USA, 1996, pp. 539-554.
[10] R.A. Oriani, Whitney Award Lecture—1987:Hydrogen—The Versatile Embrittler, Corrosion 43(7) (1987) 390-397.
[11] R.A. Oriani, P.H. Josephic, Equilibrium and kinetic studies of the hydrogen-assisted cracking of steel, Acta Metall. 25(9) (1977) 979-988.
[12] S.P. Lynch, Environmentally Assisted Cracking - Overview of Evidence for an Adsorption-Induced Localized-Slip Process, Acta Metall. 36(10) (1988) 2639-2661.
[13] S. Lynch, Hydrogen embrittlement phenomena and mechanisms, Corros. Rev. 30(3-4) (2012) 105-123.
[14] S.P. Lynch, Metallographic contributions to understanding mechanisms of environmentally assisted cracking, Metallography 23(2) (1989) 147-171.
[15] S.P. Lynch, Comments on "A unified model of environment-assisted cracking", Scr. Mater. 61(3) (2009) 331-334.
[16] Y. Fukai, Formation of superabundant vacancies in M–H alloys and some of its consequences: a review, J. Alloys Compd. 356-357 (2003) 263-269.
[17] M. Nagumo, Hydrogen related failure of steels – a new aspect, Mater. Sci. Technol. 20(8) (2013) 940-950.

[18] D.S. Shih, I.M. Robertson, H.K. Birnbaum, Hydrogen embrittlement of α titanium: In situ tem studies, Acta Metall. 36(1) (1988) 111-124.

[19] M.L. Holzworth, M.R. Louthan, Hydrogen-Induced Phase Transformations in Type 304L Stainless Steels, Corrosion 24(4) (1968) 110-124.

[20] N. Narita, C.J. Altstetter, H.K. Birnbaum, Hydrogen-related phase transformations in austenitic stainless steels, Metall. Trans. A 13(8) (1982) 1355-1365.

[21] H.K. Birnbaum, Mechanical properties of metal hydrides, J. Less Common Met. 104(1) (1984) 31-41.

[22] P. Peralta, C. Laird, Fatigue of Metals, in: D.E. Laughlin, K. Hono (Eds.), Physical Metallurgy (Fifth Edition), Elsevier, Amsterdam, 2014, pp. 1765-1880.

[23] H. Matsunaga, M. Yoshikawa, R. Kondo, J. Yamabe, S. Matsuoka, Slow strain rate tensile and fatigue properties of Cr-Mo and carbon steels in a 115 MPa hydrogen gas atmosphere, Int J Hydrog Energy 40(16) (2015) 5739-5748.

[24] Y. Ogawa, D. Birenis, H. Matsunaga, A. Thogersen, O. Prytz, O. Takakuwa, J. Yamabe, Multi-scale observation of hydrogen-induced, localized plastic deformation in fatigue-crack propagation in a pure iron, Scr. Mater. 140 (2017) 13-17.

[25] Y. Ogawa, J. Yamabe, H. Matsunaga, S. Matsuoka, Material performance of age-hardened beryllium–copper alloy, CDA-C17200, in a high-pressure, gaseous hydrogen environment, Int J Hydrog Energy 42(26) (2017) 16887-16900.

[26] M. Nakamura, S. Okazaki, H. Matsunaga, S. Matsuoka, SSRT and fatigue life properties of austenitic stainless steel weld metal 317L in high-pressure hydrogen gas, Transactions of the JSME (in Japanese) 84(857) (2018) 1-20.

[27] J. Yamabe, M. Yoshikawa, H. Matsunaga, S. Matsuoka, Hydrogen trapping and fatigue crack growth property of low-carbon steel in hydrogen-gas environment, Int. J. Fatigue 102 (2017) 202-213.

[28] H. Matsunaga, O. Takakuwa, J. Yamabe, S. Matsuoka, Hydrogen-enhanced fatigue crack growth in steels and its frequency dependence, Philosophical Transactions A 375(2098) (2017).

[29] S. Matsuoka, J. Yamabe, H. Matsunaga, Criteria for determining hydrogen compatibility and the mechanisms for hydrogen-assisted, surface crack growth in austenitic stainless steels, Eng. Fract. Mech. 153 (2016) 103-127.

[30] T.L. Anderson, Fracture Mechanics: Fundamentals and Applications, third ed., CRC Press, Boca Raton, 2005.

[31] D. Wan, Y. Deng, A. Barnoush, Hydrogen embrittlement effect observed by in-situ hydrogen plasma charging on a ferritic alloy, Scr. Mater. 151 (2018) 24-27.

[32] C.G. Morgan, R. Vane, Removal of Carbon Contamination using Hydrogen with Low-Power Downstream Plasma Cleaning. https://evactron.com/wp-content/uploads/2016/10/cleaningwithh2advlith2011.pdf, 2011).

[33] G.M. Bond, I.M. Robertson, H.K. Birnbaum, On the determination of the hydrogen fugacity in an environmental cell tem facility, Scripta Metall. 20(5) (1986) 653-658.

[34] S.-S. Rui, Y.-B. Shang, W. Qiu, L.-S. Niu, H.-J. Shi, S. Matsumoto, Y. Chuman, Fracture mode identification of low alloy steels and cast irons by electron back-scattered diffraction misorientation analysis, Journal of Materials Science & Technology 33(12) (2017) 1582-1595.

[35] S.-S. Rui, Y.-B. Shang, Y. Su, W. Qiu, L.-S. Niu, H.-J. Shi, S. Matsumoto, Y. Chuman, EBSD analysis of cyclic load effect on final misorientation distribution of post-mortem low alloy steel: A new method for fatigue crack tip driving force prediction, Int. J. Fatigue 113 (2018) 264-276.

[36] H. Vehoff, P. Neumann, In situ sem experiments concerning the mechanism of ductile crack growth, Acta Metall. 27(5) (1979) 915-920.

[37] C. Laird, G.C. Smith, Crack propagation in high stress fatigue, Philos. Mag. 7(77) (1962) 847-857.

[38] S.S. Chakravarthy, W.A. Curtin, Origin of plasticity length-scale effects in fracture, Phys. Rev. Lett. 105(11) (2010) 115502.

[39] M. Nagumo, K. Miyamoto, Microscopic Process of Failure and Mechanism of Hydrogen Embrittlement of Iron, J. Jpn. Inst. Met. 45(12) (1981) 1309-1317.

[40] M. Nagumo, T. Takahashi, Hydrogen embrittlement of some Fe-base amorphous alloys, Mater. Sci. Eng. 23(2-3) (1976) 257-259.

[41] Y. Ogawa, D. Birenis, H. Matsunaga, O. Takakuwa, J. Yamabe, Ø. Prytz, A. Thøgersen, Hydrogen-assisted fatigue crack propagation in a pure BCC iron. Part I: Intergranular crack propagation at relatively low stress intensities, MATEC Web of Conferences 165 (2018) 03011.

[42] Y. Ogawa, H. Matsunaga, J. Yamabe, M. Yoshikawa, S. Matsuoka, Unified evaluation of hydrogen-induced crack growth in fatigue tests and fracture toughness tests of a carbon steel, Int. J. Fatigue 103 (2017) 223-233.

[43] Y. Ogawa, H. Matsunaga, M. Yoshikawa, J. Yamabe, S. Matsuoka, Fatigue Life Properties and Anomalous Macroscopic Fatigue Fracture Surfaces of Low Carbon Steel JIS-SM490B in High-Pressure Hydrogen Gas Environment, ASME 2016 Pressure Vessels and Piping Conference, 2016, p. V06BT06A027.

[44] F. Terasaki, T. Kawakami, A. Yoshikawa, N. Takano, Mechanism of crack propagation due to hydrogen embrittlement in iron single crystals stressed along [001] axis, Revue de Métallurgie 95(12) (2017) 1519-1529.

[45] H. Vehoff, W. Rothe, Overview .30. Gaseous-Hydrogen Embrittlement in Fesi-Single and Ni-Single Crystals, Acta Metall. 31(11) (1983) 1781-1793.

[46] D. Wan, A. Alvaro, V. Olden, A. Barnoush, Hydrogen-assisted fatigue crack growth in ferritic steels – a fractographic study, MATEC Web of Conferences, 2018, p. 03004.

[47] D. Birenis, Y. Ogawa, H. Matsunaga, O. Takakuwa, J. Yamabe, Ø. Prytz, A. Thøgersen, Interpretation of hydrogen-assisted fatigue crack propagation in BCC iron based on dislocation structure evolution around the crack wake, Acta Mater. 156 (2018) 245-253.

[48] Y. Deng, A. Barnoush, Hydrogen embrittlement revealed via novel in situ fracture experiments using notched micro-cantilever specimens, Acta Mater. 142 (2018) 236-247.

[49] B.R.S. Rogne, N. Kheradmand, Y. Deng, A. Barnoush, In situ micromechanical testing in environmental scanning electron microscope: A new insight into hydrogen-assisted cracking, Acta Mater. 144 (2018) 257-268.

[50] T. Hajilou, Y. Deng, B.R. Rogne, N. Kheradmand, A. Barnoush, In situ electrochemical microcantilever bending test: A new insight into hydrogen enhanced cracking, Scr. Mater. 132 (2017) 17-21.

[51] S. Taketomi, R. Matsumoto, N. Miyazaki, Atomistic study of hydrogen distribution and diffusion around a {112}<111> edge dislocation in alpha iron, Acta Mater. 56(15) (2008) 3761-3769.

[52] Y. Murakami, T. Kanezaki, Y. Mine, Hydrogen Effect against Hydrogen Embrittlement, Metall. Mater. Trans. A 41(10) (2010) 2548-2562.

[53] R. Kirchheim, Solid solution softening and hardening by mobile solute atoms with special focus on hydrogen, Scr. Mater. 67(9) (2012) 767-770.

[54] S. Puydebois, A. Oudriss, P. Bernard, L. Briottet, X. Feaugas, Hydrogen effect on the fatigue behavior of LBM Inconel 718, MATEC Web of Conferences 165 (2018) 02010.

[55] T. Matsuo, S. Matsuoka, Y. Murakami, Fatigue crack growth properties of quenched and tempered Cr-Mo steel in 0.7 MPa hydrogen gas, The 18th European Conference on Fracture: Fracture of Materials and Structures from Micro to Macro Scale, Dresden, Germany, 2010.

[56] M. Yoshikawa, T. Matsuo, N. Tsutsumi, H. Matsunaga, S. Matsuoka, Effects of hydrogen gas pressure and test frequency on fatigue crack growth properties of low carbon steel in 0.1-90 MPa hydrogen gas, Transactions of the JSME 80(817) (2014) SMM0254.

[57] P. Sofronis, R.M. McMeeking, Numerical analysis of hydrogen transport near a blunting crack tip, J. Mech. Phys. Solids 37(3) (1989) 317-350.

[58] H. Kotake, R. Matsumoto, S. Taketomi, N. Miyazaki, Transient hydrogen diffusion analyses coupled with crack-tip plasticity under cyclic loading, International Journal of Pressure Vessels and Piping 85(8) (2008) 540-549.
[59] K. Kiuchi, R.B. McLellan, The solubility and diffusivity of hydrogen in well-annealed and deformed iron, Acta Metall. 31(7) (1983) 961-984.
[60] D. Hull, D.J. Bacon, Introduction to Dislocations 5th Edition, Elsevier, Amsterdam, 2011.

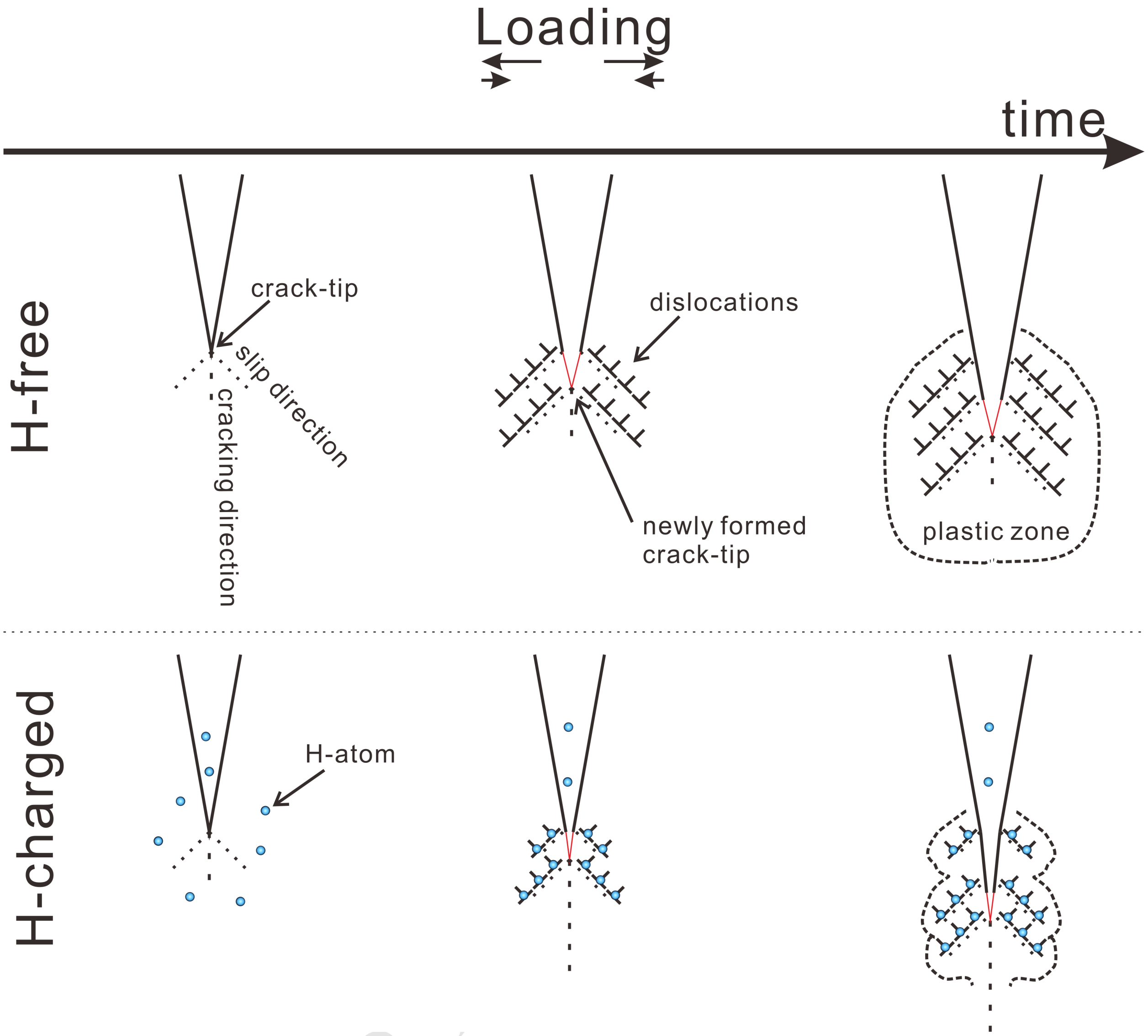
Loading
time
H-free
crack-tip
slip direction
cracking direction
dislocations
newly formed
crack-tip
plastic zone
H-charged
H-atom

ACCEP

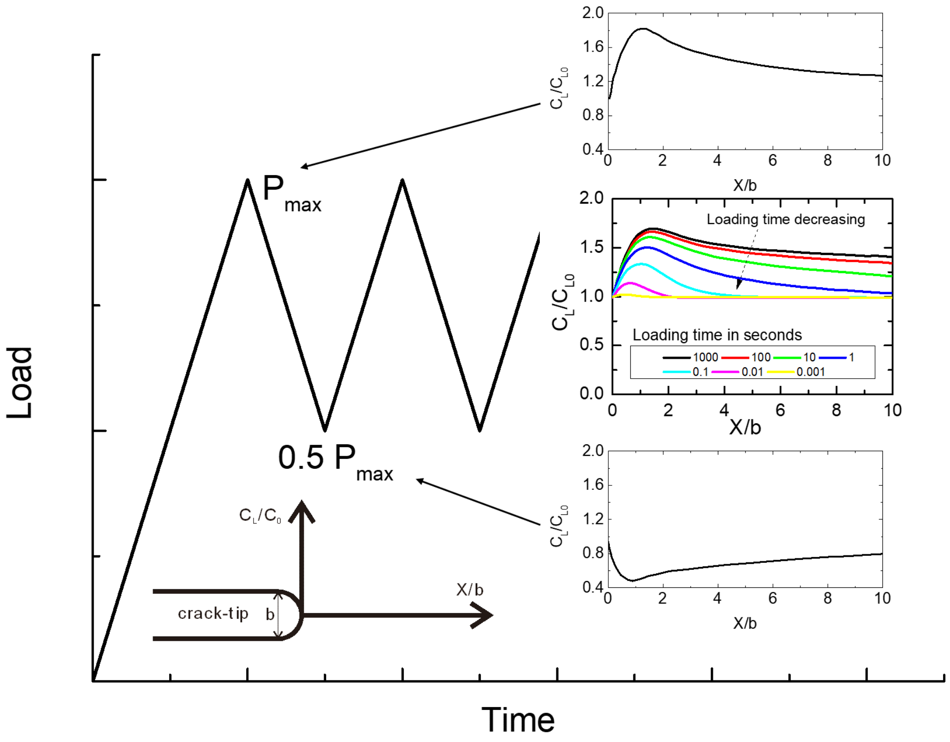
Load
Time
P_{max}
$0.5\ P_{max}$
C_L/C_0
X/b
crack-tip
b
C_L/C_{L0}
X/b
Loading time decreasing
Loading time in seconds
1000
100
10
1
0.1
0.01
0.001
2.0
1.6
1.2
0.8
0.4
1.5
1.0
0.5
0.0
0
2
4
6
8
10

ACCEPTED M

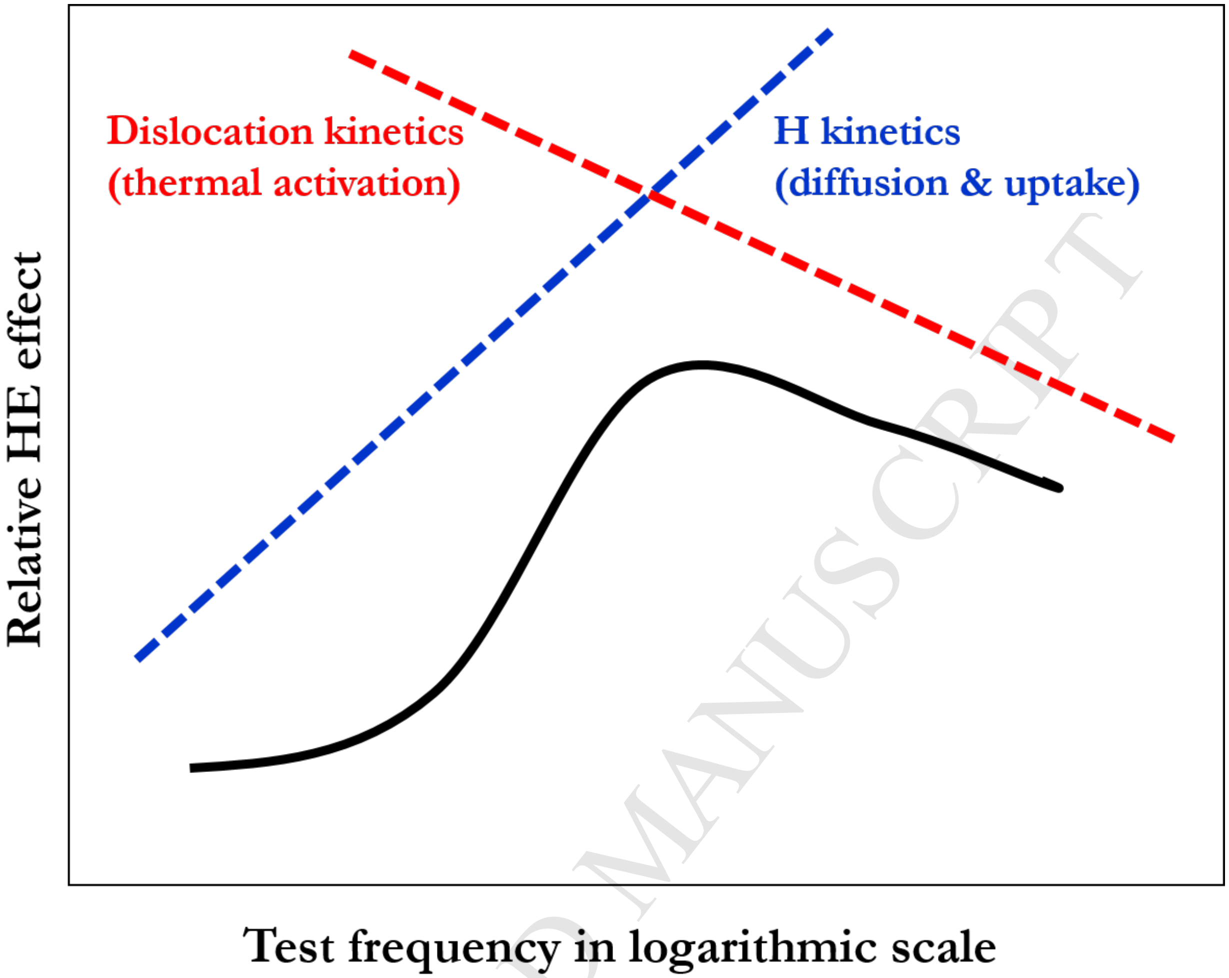
Dislocation kinetics
(thermal activation)
H kinetics
(diffusion & uptake)
Relative HE effect
Test frequency in logarithmic scale

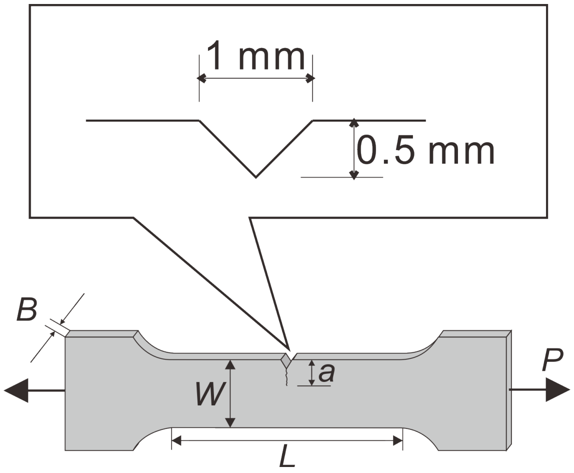
1 mm
0.5 mm
B
P
a
W
L

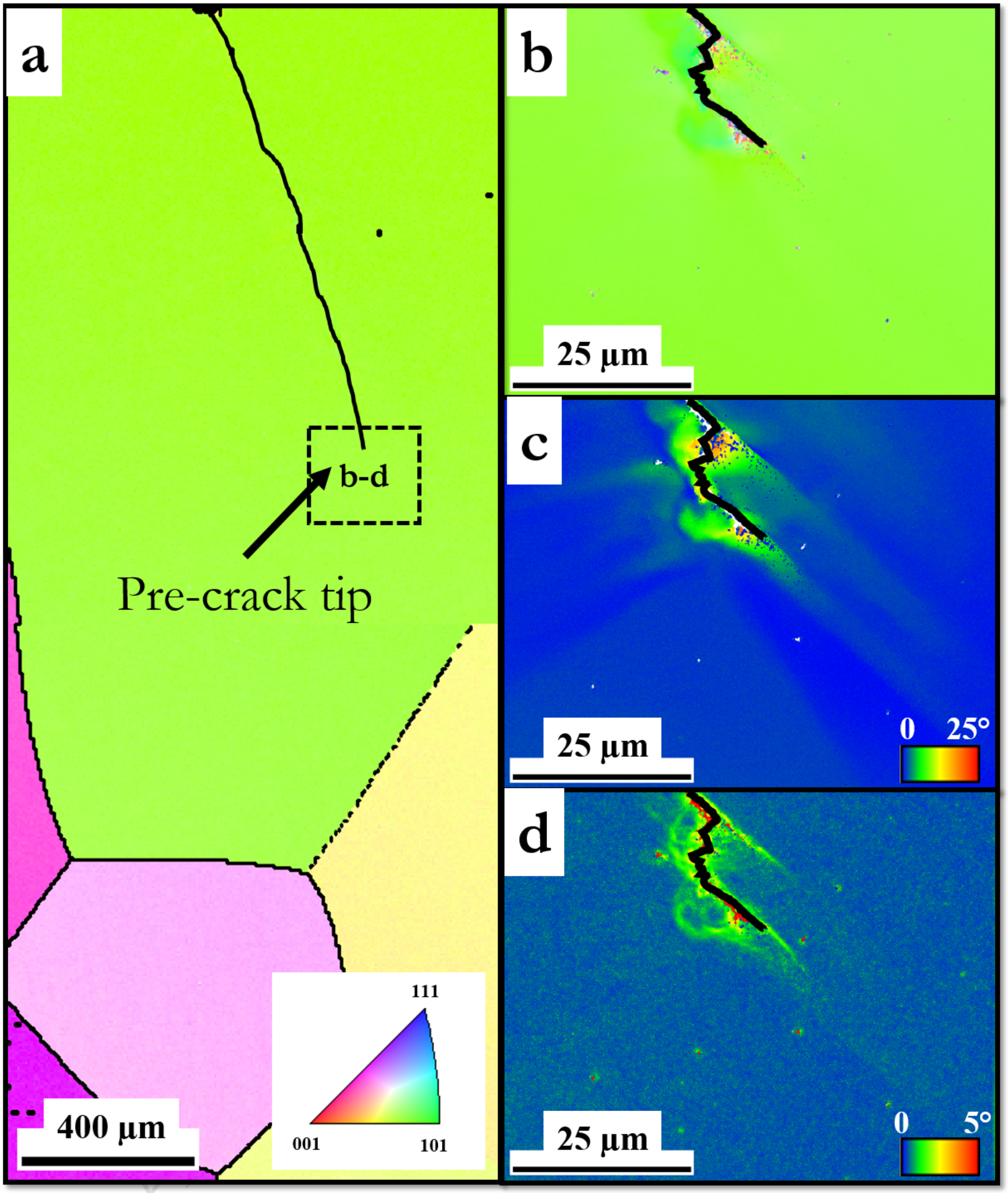
a
b-d
Pre-crack tip
400 µm
111
001
101
b
25 µm
c
25 µm
0
25°
d
25 µm
0
5°

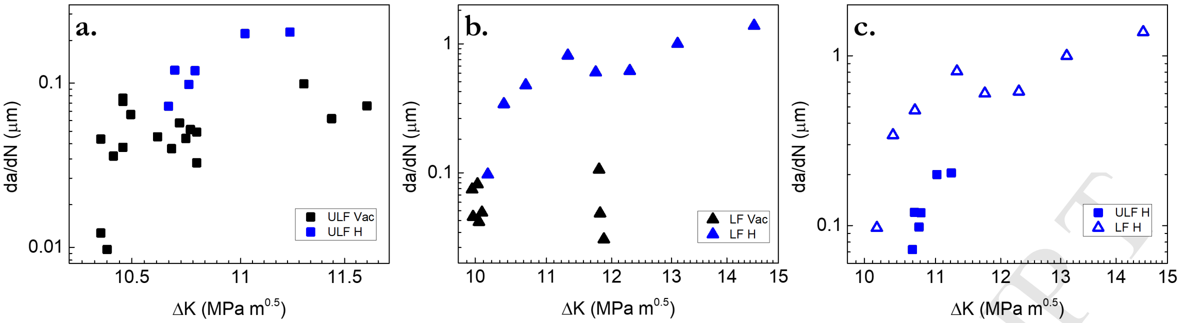
a.
da/dN (μm)
0.1
0.01
10.5
11
11.5
ΔK (MPa m^0.5)
ULF Vac
ULF H
b.
da/dN (μm)
1
0.1
10
11
12
13
14
15
ΔK (MPa m^0.5)
LF Vac
LF H
c.
da/dN (μm)
1
0.1
10
11
12
13
14
15
ΔK (MPa m^0.5)
ULF H
LF H

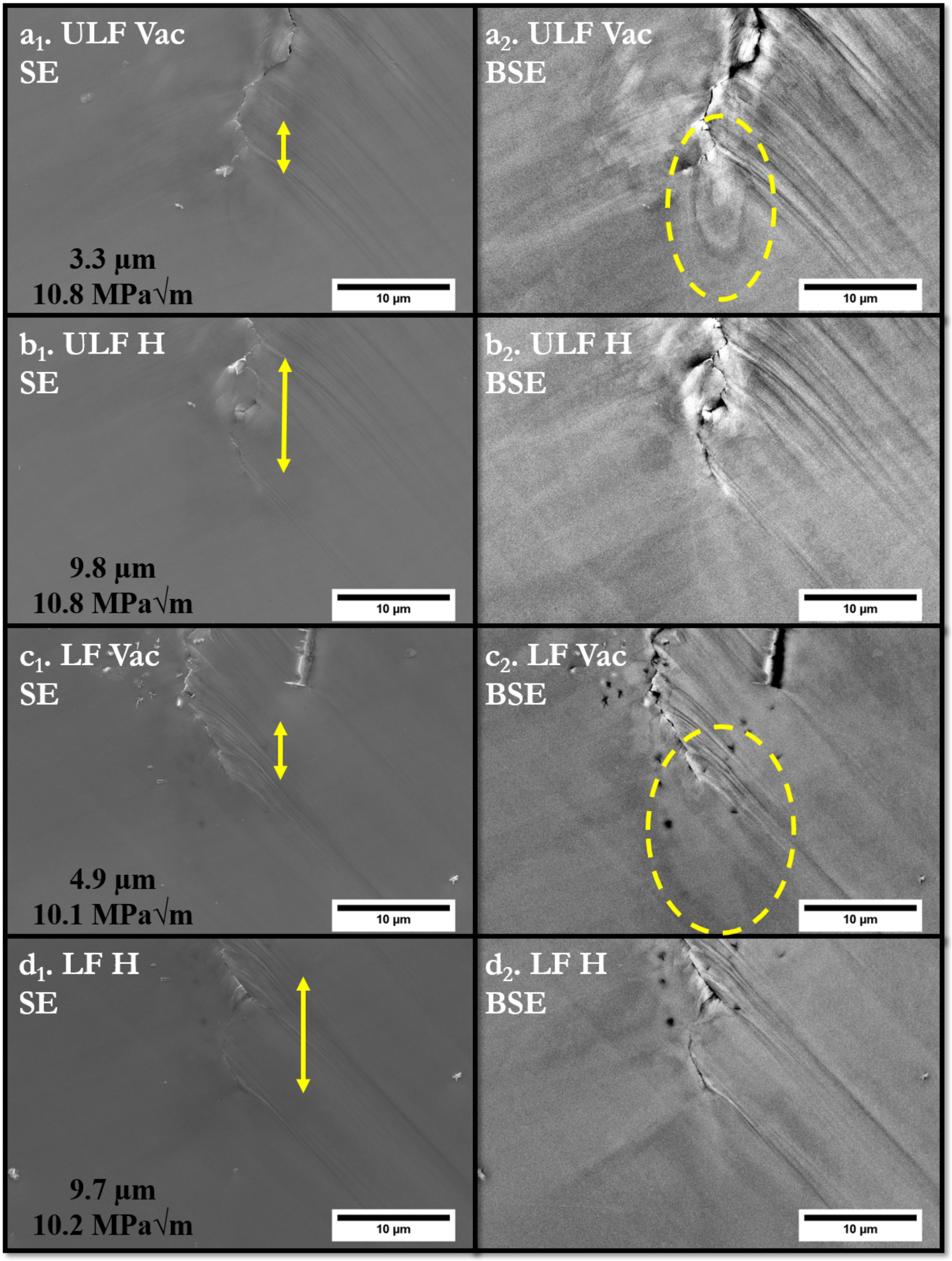
a1. ULF Vac
SE
3.3 µm
10.8 MPa√m
10 µm
a2. ULF Vac
BSE
10 µm
b1. ULF H
SE
9.8 µm
10.8 MPa√m
10 µm
b2. ULF H
BSE
10 µm
c1. LF Vac
SE
4.9 µm
10.1 MPa√m
10 µm
c2. LF Vac
BSE
10 µm
d1. LF H
SE
9.7 µm
10.2 MPa√m
10 µm
d2. LF H
BSE
10 µm

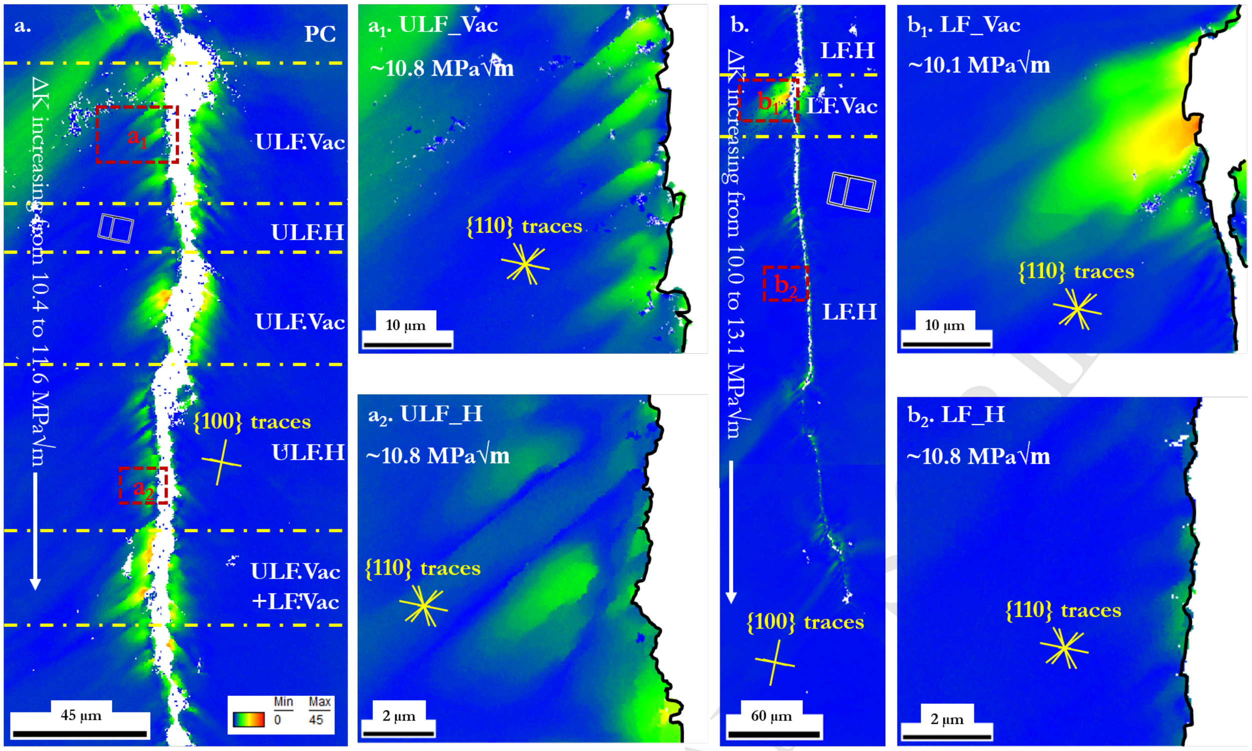
a.
PC
ULF.Vac
ULF.H
ULF.Vac
{100} traces
ULF.H
ULF.Vac
+LF.Vac
ΔK increasing from 10.4 to 11.6 MPa√m
a_1
a_2
45 μm
Min 0
Max 45
a_1. ULF_Vac
~10.8 MPa√m
{110} traces
10 μm
a_2. ULF_H
~10.8 MPa√m
{110} traces
2 μm
b.
LF.H
LF.Vac
LF.H
ΔK increasing from 10.0 to 13.1 MPa√m
b_1
b_2
{100} traces
60 μm
b_1. LF_Vac
~10.1 MPa√m
{110} traces
10 μm
b_2. LF_H
~10.8 MPa√m
{110} traces
2 μm

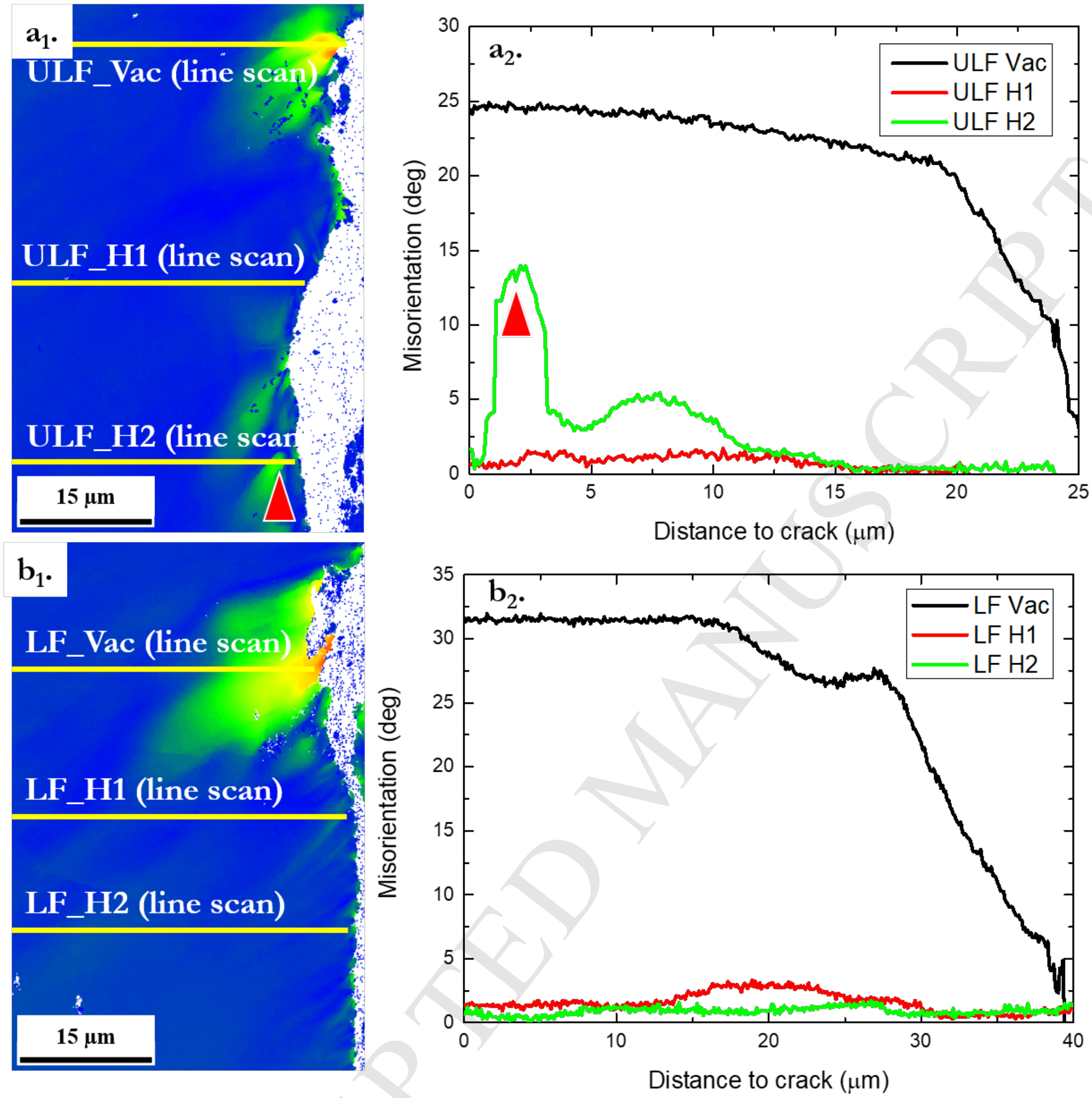
a1.
ULF_Vac (line scan)
ULF_H1 (line scan)
ULF_H2 (line scan)
15 μm
a2.
ULF Vac
ULF H1
ULF H2
Misorientation (deg)
Distance to crack (μm)
0
5
10
15
20
25
30
b1.
LF_Vac (line scan)
LF_H1 (line scan)
LF_H2 (line scan)
15 μm
b2.
LF Vac
LF H1
LF H2
Misorientation (deg)
Distance to crack (μm)
0
10
20
30
40
35

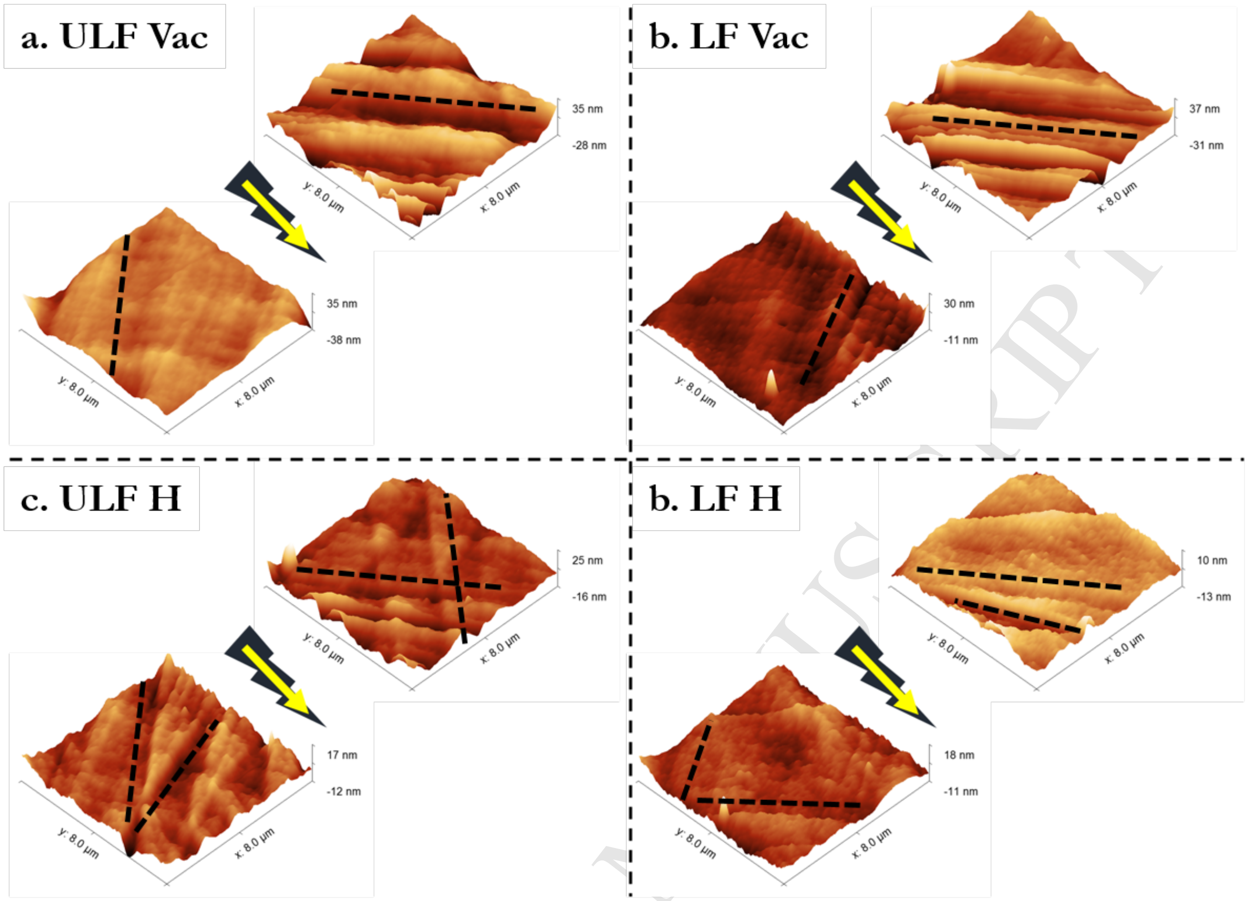
a. ULF Vac
35 nm
-28 nm
y: 8.0 µm
x: 8.0 µm
35 nm
-38 nm
y: 8.0 µm
x: 8.0 µm
b. LF Vac
37 nm
-31 nm
y: 8.0 µm
x: 8.0 µm
30 nm
-11 nm
y: 8.0 µm
x: 8.0 µm
c. ULF H
25 nm
-16 nm
y: 8.0 µm
x: 8.0 µm
17 nm
-12 nm
y: 8.0 µm
x: 8.0 µm
b. LF H
10 nm
-13 nm
y: 8.0 µm
x: 8.0 µm
18 nm
-11 nm
y: 8.0 µm
x: 8.0 µm

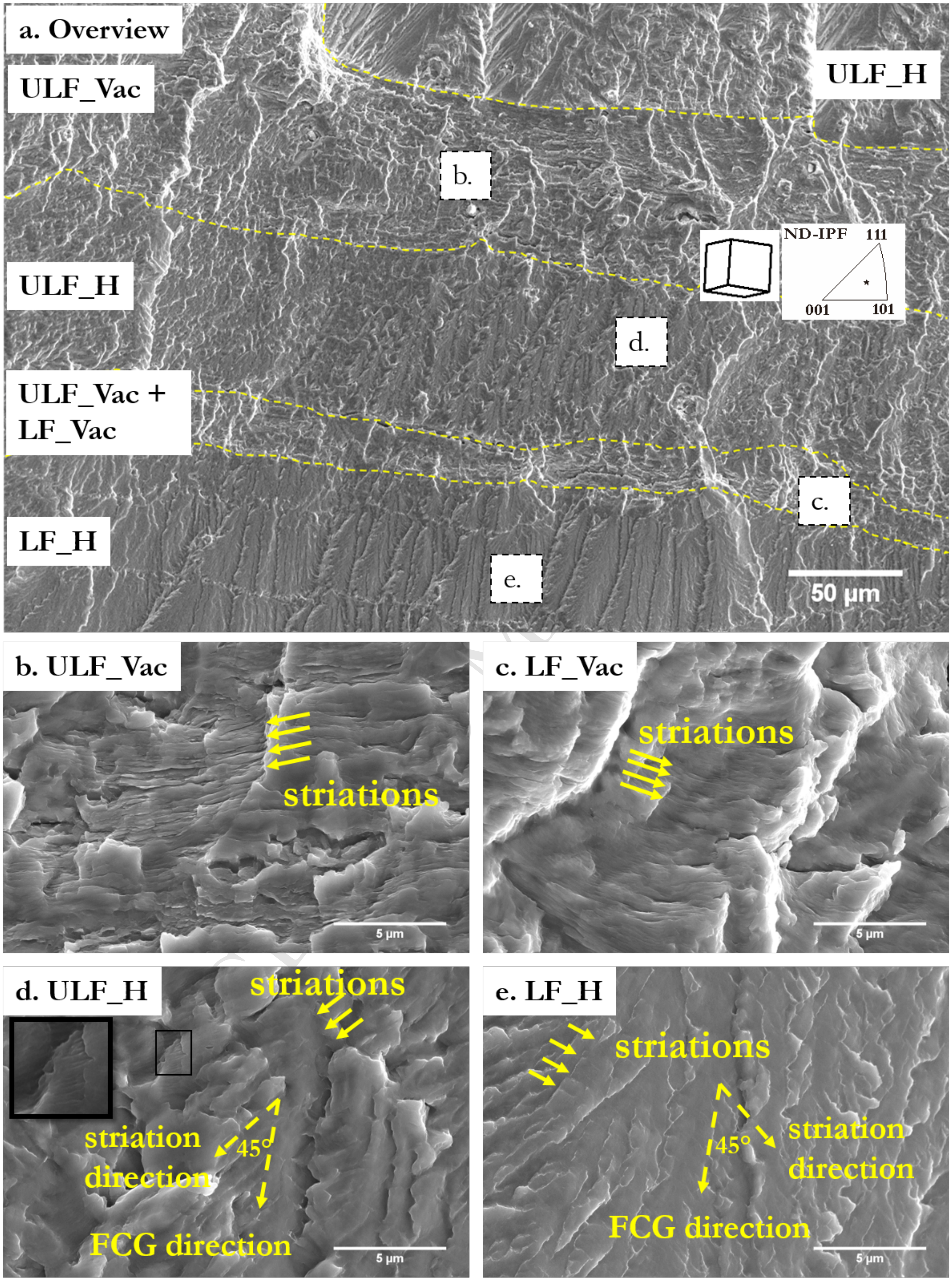
a. Overview
ULF_Vac
ULF_H
ULF_H
ULF_Vac +
LF_Vac
LF_H
b.
c.
d.
e.
ND-IPF
111
001
101
50 µm
b. ULF_Vac
striations
5 µm
c. LF_Vac
striations
5 µm
d. ULF_H
striations
striation
direction
45°
FCG direction
5 µm
e. LF_H
striations
45°
striation
direction
FCG direction
5 µm

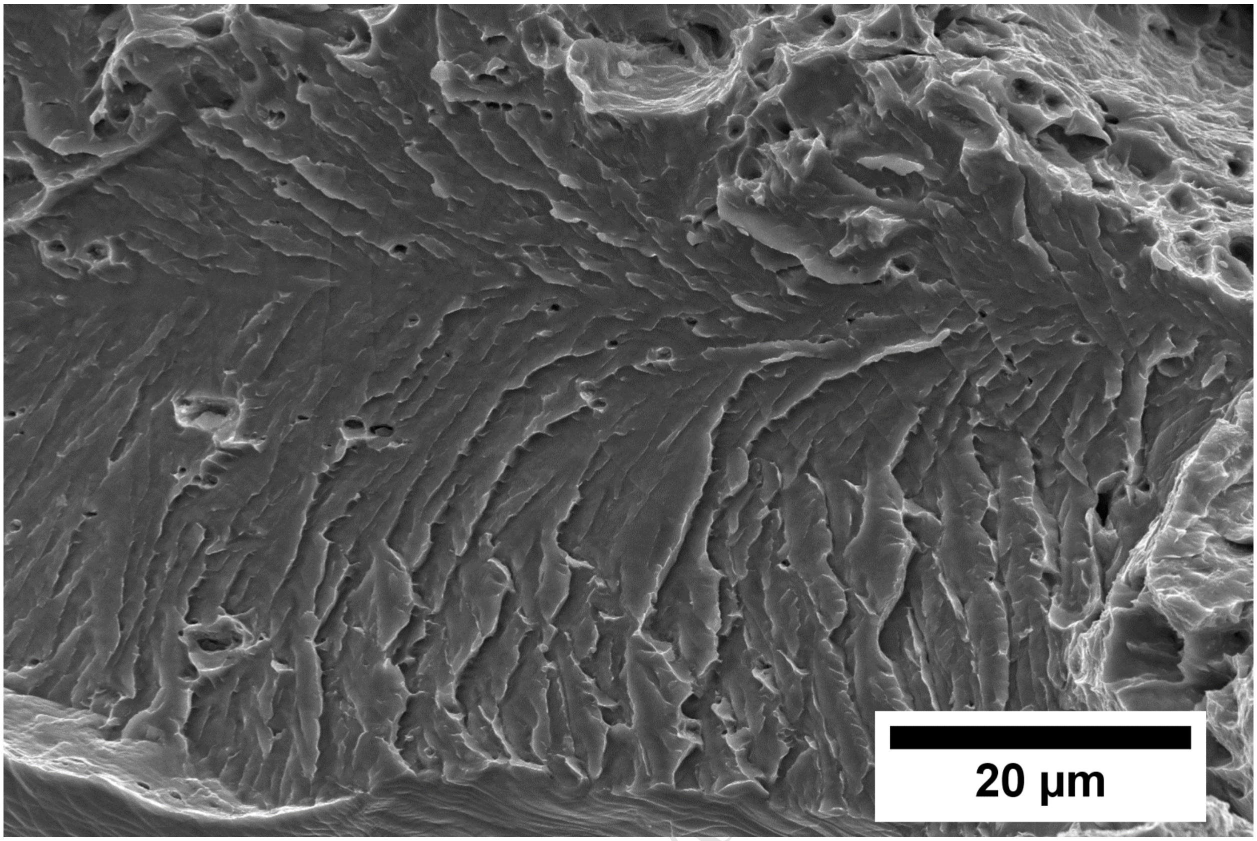
20 µm